MOX-Report No. 06/2023

A segregated finite volume - spectral element method for aeroacoustic problems

Artoni, A.; Antonietti, P. F.; Mazzieri, I.; Parolini, N.; Rocchi, D.

MOX, Dipartimento di Matematica
Politecnico di Milano, Via Bonardi 9 - 20133 Milano (Italy)

mox-dmat@polimi.it https://mox.polimi.it

A segregated finite volume - spectral element method for aeroacoustic problems

Alberto Artoni[1,*], Paola F. Antonietti[1], Ilario Mazzieri[1], Nicola Parolini[1], and Daniele Rocchi[2]

[1]MOX-Laboratory for Modeling and Scientific Computing, Department of Mathematics, Politecnico di Milano, 20133 Milan, Italy
[2]Department of Mechanical Engineering, Politecnico di Milano, 20156 Milan, Italy

[*]Corresponding author: alberto.artoni@polimi.it

February 6, 2023

Abstract

We propose a segregated Finite Volume (FV) - Spectral Element Method (SEM) for modelling aeroacoustic phenomena based on the Lighthill's acoustic analogy. First the fluid solution is computed employing a FV method. Then, the sound source term is projected onto the acoustic grid and the inhomogeneous Lighthill's wave equation is solved employing the SEM. The novel projection method computes offline the intersections between the acoustic and the fluid grids in order to preserve the accuracy. The proposed intersection algorithm is shown to be robust, scalable and able to efficiently compute the geometric intersection of arbitrary polyhedral elements. We then analyse the properties of the projection error and we numerically assess the obtained theoretical estimates. Finally, we address two relevant aeroacoustic benchmarks, namely the corotating vortex pair and the noise induced by a laminar flow around a squared cylinder, to demonstrate in practice the effectiveness of the proposed approach. The flow computations are performed with OpenFOAM [46], an open-source finite volume library, while the inhomogeneous Lighthill's wave equation is solved with SPEED [31], an open-source spectral element library.

1 Introduction

Aeroacoustics studies the propagation of noise generated by fluid flows. A typical problem of interest can be the noise induced by a car side view mirror. For a car moving at $40\,\mathrm{m\,s^{-1}}$, the corresponding Reynolds number is of the order of 10^6. The typical mesh size required to capture the fluid length scales (even when working with turbulence models) are of the order of 10^{-3}m or 10^{-4}m [45], far from the involved acoustic scales that range from $0.05\,\mathrm{m}$ up to $5\,\mathrm{m}$, see for instance [19]. Due to the multiscale nature of the involved length scales, a widely employed class of Computational Aeroacoustics (CAA) methodologies separate

the flow field from the acoustic computations, in a segregated approach. Those methods are based on aeroacoustic analogies, namely rearrangement of the mass and momentum conservation laws of the flow, and are well suited for segregated computations. The main idea is to feed in a one-way coupling the sound noise source induced by the flow field to an acoustic transport problem, see for instance Figure 1. Since the first development of aeroacoustics, segregated methods have been established as a practical method for fast and accurate predictions for certain flow problems. In the aeroacoustic community, this kind of segregated approach is called hybrid strategy. From now on, we employ the term hybrid as a synonym of the term segregated.

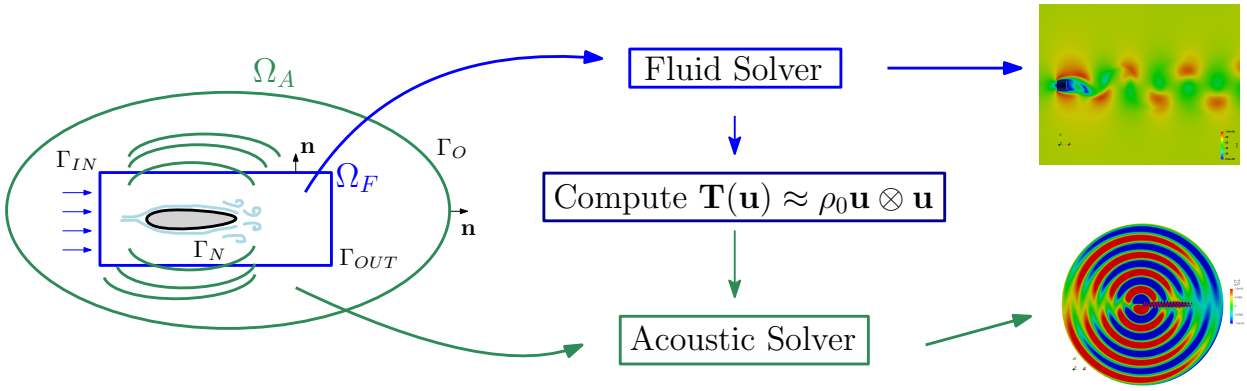

Figure 1: Computational domain for the aeroacoustic problem and sketch of the segregated numerical strategy. First, the fluid problem is solved on Ω_F. Then the acoustic source term is computed from the flow velocity. Finally, an inhomogeneous acoustic wave equation is solved on Ω_A.

In this work, we consider problems with high speed flow velocity, low Mach number and in which we assume that there is no interaction between the fluid pressure and the acoustic pressure, namely, where the one-way coupling hypothesis holds. Examples of physical relevance where such assumptions are verified and where recently hybrid methods have been successfully applied are [25, 23] for subsonic flows, [2, 48, 16] for human phonation and [15] for airframe noise at low Mach. The greatest advantage of segregated computational strategies for aeroacoustic problems is the possibility of choosing the optimal computational grids and optimal numerical methods for both the acoustic problem and the flow problem. In the flow problem, sufficiently fine computational grid to resolve the turbulence or wall scales must be employed in order to properly describe the underlying physics of the flow. For the acoustic problem, the domain is usually much bigger and the involved acoustic pressure length scales are larger. Moreover, the sound generation mechanism can be often confined only to the fluid region, allowing the acoustic problem to be modelled as a pure wave propagation problem. With this setting, optimal computational methods can be chosen for each problem independently. In this work, we propose to employ Finite Volumes (FV) schemes for the fluid problem. The corresponding FV solution is the employed to compute the source term for the acoustic wave propagation problem, which is then solved employing Spectral Element Methods (SEM). High order approximation have already been employed in computational aeroacoustic, see for instance [21] and [38]. A critical step in hybrid methods is the coupling between the fluid and the acoustic domain, and how the noise source field is interpolated between the computational grids. We remark that the fluid and acoustic grids might have very different granularities in order to capture the underlying (different) physics. While simple nearest neighbour interpolation fails to compute the acoustic sources

accurately [7], conservative interpolation schemes lack of important analytical framework, although have been successfully employed, see for instance [26]. The L^2-projection method has been employed on nested Cartesian grids by [38], although the use of Cartesian grids is not suitable for most of industrial applications, where complex geometries are involved. In this work, we generalize the method to arbitrary polyhedral grids, proposing an efficient algorithm to compute the intersections between the fluid and acoustic elements. We then compute the projection of the sound source term computed as a post-process of the flow solution onto the acoustic grid by employing a quadrature free method on polyhedral elements. The proposed coupling strategy is flexible and acts as a black box, requiring only the sound source term at the cell centre of the fluid cell. Furthermore, it is naturally suited for high order approximations since the employed quadrature formula integrates exactly arbitrary polynomials. We provide a rigorous theoretical analysis quantifying the effect of the projection error. The theoretical results are then validated by means of numerical experiments. The flow computations are performed with OpenFOAM [46], an open-source finite volume library, while the inhomogeneous acoustic wave equation is solved with SPEED [31], an open-source spectral element library.
The paper is structured as follows. In Section 2 we introduce the aeroacoustic hybrid problem, and we propose our strategy to solve the inhomogeneous Lighthill's wave equation. We focus our attention on the coupling between the fluid and acoustic problem. We develop in Section 3 the theoretical analysis on the projection method and we then discuss in Section 4 the challenging implementation aspects. In Section 5 we test the proposed intersection algorithm and we verify in Section 6 the theoretical estimates for the projection error. In Section 7 we apply the proposed computational strategy on benchmark aeroacoustic problems.

2 The aeroacoustic model problem

In the literature, it is possible to find a wide variety of aeroacoustic models: from semi-analytical strategies based on employing suitable Green functions that led to the popular Curle [9] and Ffowcs Williams Hawkings analogies [18], to more recent models that aim to solve the acoustic perturbed equations (APE), see for instance [15]. Most of the approximation methods proposed for these models rely on a hybrid strategy: first, they compute the fluid flow solution and then, they solve the acoustic problem using the latter to compute the sound source. This is the principle upon which the Lighthill's wave equation is based on.

2.1 Lighthill's wave equation

Let $\Omega \subset \mathbb{R}^3$, be a connected open bounded domain with sufficiently smooth boundary $\partial\Omega$. We denote by $\mathbf{x} \in \Omega$ the vector of spatial coordinates, and by $t \in (0, T]$ the time coordinate, being $T > 0$ a final observation time. We consider in $\Omega \times (0, T]$ the compressible unsteady Navier-Stokes equations:

$$\frac{\partial \rho}{\partial t} + \nabla \cdot (\rho \mathbf{u}) = 0, \tag{1}$$

$$\frac{\partial \rho \mathbf{u}}{\partial t} + \nabla \cdot (\rho \mathbf{u} \otimes \mathbf{u}) = -\nabla p + \nabla \cdot \boldsymbol{\sigma}, \tag{2}$$

$$\frac{\partial \rho E}{\partial t} + \nabla \cdot [(\rho E + p)\mathbf{u}] = \nabla \cdot (\boldsymbol{\sigma}\mathbf{u} - \mathbf{q}), \tag{3}$$

supplemented with suitable boundary and initial conditions that will be detailed later on. Equations (1), (2) and (3) are the mass, momentum and energy balance equations, respectively, where $\boldsymbol{\sigma}$ denotes the viscous stress tensor, ρ is the fluid density, p is the pressure, $\mathbf{u}$ is the velocity, ρE is the total energy and $\mathbf{q}$ is the heat flux. We define the non dimensional Mach (Ma) and Reynolds (Re) numbers as

$$\mathrm{Ma} = \frac{U}{c_0}, \qquad \mathrm{Re} = \frac{UL}{\nu},$$

where U is the characteristic speed of the flow, c_0 is the speed of sound, L is the characteristic length of the flow problem, and ν is the kinematic viscosity. We derive the Lighthill's wave equation, see [28], by taking the time derivative of (1) and subtracting the divergence of the momentum equation (2). Then, we have

$$\frac{\partial^2 \rho}{\partial t^2} = \nabla \cdot \nabla \cdot (\rho \mathbf{u} \otimes \mathbf{u} + p\mathbf{I} - \boldsymbol{\sigma}).$$

Summing and subtracting in the above equation the term $c_0^2 \Delta \rho$, we obtain the following wave equation:

$$\frac{\partial^2 \rho}{\partial t^2} - c_0^2 \Delta \rho = \nabla \cdot \nabla \cdot \mathbf{T}, \tag{4}$$

where the right-hand side has been reformulated by introducing the so-called Lighthill's tensor

$$\mathbf{T} = \rho \mathbf{u} \otimes \mathbf{u} + (p - c_0^2 \rho)\mathbf{I} - \boldsymbol{\sigma}, \tag{5}$$

being $\mathbf{I}$ the identity tensor. Model problem (4)-(5) can be further simplified depending on the problem of interest. For a sufficiently high Reynolds number, it is possible to neglect the viscous source term in the Lighthill's tensor. Assuming a low Mach number and no combustion effects, the fluid can be considered isentropic, leading to $p = c_0^2 \rho$. Under these assumptions, the Lighthill's tensor in (5) reduces to $\mathbf{T} = \rho_0 \mathbf{u} \otimes \mathbf{u}$, where ρ_0 is a reference density for the fluid. This leads to the following wave equation:

$$\frac{\partial^2 \rho}{\partial t^2} - c_0^2 \Delta \rho = \nabla \cdot \nabla \cdot (\rho_0 \mathbf{u} \otimes \mathbf{u}), \tag{6}$$

which describes the evolution of a density wave in a quiescent material where the speed of propagation is given by c_0, the fluid density is given by ρ_0 and the sound source is given by the approximation of the Lighthill's stress tensor. Equation 6 is then supplemented with suitable initial and boundary conditions, as detailed in the following.

2.2 The hybrid coupled model problem

With the aim of studying aeroacoustic problems related to the noise generated by external flows around bodies, we consider the following setup. We assume acoustic compactness, which means that the size of the flow source structures that generate the acoustic field are small compared to the acoustic generated wavelength. This hypothesis is inherently fulfilled for low Mach number applications. Next, we consider a connected domain Ω_F, having sufficiently regular boundary $\partial\Omega_F$, embedded in a connected domain Ω_A, with sufficiently regular boundary $\partial\Omega_A$, see Figure 1.

The segregated algorithm requires to solve the following sequence of problems:
1. Fluid Problem. For the fluid problem we consider the incompressible Navier Stokes

equations, that read as
for $t \in (0,T]$, find $\mathbf{u}(\mathbf{x},t) : \Omega_F \times (0,T] \to \mathbb{R}^3$ and $p(\mathbf{x},t) : \Omega_F \times (0,T] \to \mathbb{R}$ such that

$$\begin{aligned}
\frac{\partial \mathbf{u}}{\partial t} + (\mathbf{u}\cdot\nabla)\mathbf{u} - \nabla\cdot(\nu\nabla\mathbf{u}) + \nabla(\frac{p}{\rho_0}) = 0, &\quad \text{in } \Omega_F \times (0,T],\\
\nabla\cdot\mathbf{u} = 0, &\quad \text{in } \Omega_F \times (0,T],\\
\mathbf{u}(\mathbf{x},0) = \mathbf{0}, &\quad \text{in } \Omega_F,\\
\mathbf{u} = \mathbf{0}, &\quad \text{on } \Gamma_N,\\
\mathbf{u} = \mathbf{g}, &\quad \text{on } \Gamma_{IN},\\
\nu\nabla\mathbf{u}\cdot\mathbf{n} - p\mathbf{n} = \mathbf{0}, &\quad \text{on } \Gamma_{OUT},
\end{aligned} \tag{7}$$

where $\mathbf{n}$ is the outward unit normal vector to $\partial\Omega_F$, ν is the kinematic viscosity, ρ_0 is the fluid density and $\mathbf{g}$ is the inlet Dirichlet datum. Here, we suppose the fluid boundary to be decomposed as $\partial\Omega_F = \Gamma_{IN} \cup \Gamma_{OUT} \cup \Gamma_N$ such that $\Gamma_{IN} \cap \Gamma_{OUT} \cap \Gamma_N = \varnothing$.

2. Acoustic Source. From the fluid velocity $\mathbf{u}$ we define the Lighthill's tensor as $\mathbf{T} = \rho_0 \mathbf{u} \otimes \mathbf{u}$. The Lighthill's tensor has support only on the fluid domain $\Omega_F \subseteq \Omega_A$, and it depends on the solution $\mathbf{u}$ of problem (7), being the coupling term between the flow problem (7) and the acoustic problem (8).

3. Acoustic Problem. We consider in Ω_A the following non-homogeneous acoustic problem based on the Lighthill's wave equation, cf. Section 2.1: for $t \in (0,T]$, find $\rho(\mathbf{x},t) : \Omega_A \times (0,T] \to \mathbb{R}$ such that

$$\begin{aligned}
\frac{\partial^2\rho}{\partial t^2} - c_0^2\Delta\rho = \nabla\cdot\nabla\cdot\mathbf{T}, &\qquad \text{in } \Omega_A \times (0,T),\\
c_0^2\frac{\partial\rho}{\partial\mathbf{n}} = 0, &\qquad \text{on } \Gamma_N \times (0,T),\\
\frac{1}{\rho_0}\frac{\partial\rho}{\partial\mathbf{n}} = -\frac{1}{\rho_0 c_0}\frac{\partial\rho}{\partial t}(\mathbf{x},t), &\qquad \text{on } \Gamma_O \times (0,T),\\
\rho(\mathbf{x},0) = 0, &\qquad \mathbf{x} \in \Omega_A,\\
\frac{\partial\rho}{\partial t}(\mathbf{x},0) = 0, &\qquad \mathbf{x} \in \Omega_A,
\end{aligned} \tag{8}$$

where c_0 is the speed of propagation of the wave and ρ_0 is the fluid density. The boundary $\partial\Omega_A$ has been split as $\partial\Omega_A = \Gamma_O \cup \Gamma_N$. On the external boundary Γ_O, cf. Figure 1, we apply non-reflective boundary conditions, see [13], while on Γ_N we set a sound hard boundary condition, modelling a rigid wall. Initial conditions are set to zero. We are aware that the validity of this hybrid strategy and the underlying one-way coupling assumption is strongly problem-specific, depending on the geometry of the problem and the flow features. However, this approach is widely used in the context of aeroacoustics simulations, see for instance [25, 23, 48, 15].

2.3 Discretization of the incompressible Navier Sokes equations

The fluid flow problem is solved by employing the library OpenFOAM [46], an opensource library based on the cell centered finite volume method [17]. We consider a polyhedral tessellation $\mathcal{T}_F$ of the domain Ω_F and we indicate with $\mathbf{x}_0^{\kappa_F}$ the barycentre of the convex polyhedral cell $\kappa_F \in \mathcal{T}_F$. Then, we introduce the space of piecewise constant functions $V_F =$

$\{v_F \in L^2(\Omega_F) : v_F|_{\kappa_F} \in \mathbb{P}^0(\kappa_F), \forall \kappa_F \in \mathcal{T}_F\}$ with $N_F = \dim V_F$ and we denote with $\boldsymbol{V}_F = [V_F]^3$ the vector valued discrete space. In order to obtain a finite volume discretization of problem (7), we integrate the momentum equation over the polyhedron $\kappa_F \in \mathcal{T}_F$, getting

$$\int_{\kappa_F} \frac{\partial \mathbf{u}}{\partial t} d\mathbf{x} + \int_{\kappa_F} \nabla \cdot (\mathbf{u} \otimes \mathbf{u}) d\mathbf{x} - \int_{\kappa_F} \nabla \cdot (\nu \nabla \mathbf{u}) d\mathbf{x} + \int_{\kappa_F} \nabla \left(\frac{p}{\rho_0} \right) d\mathbf{x} = 0, \tag{9}$$

$$\int_{\kappa_F} \nabla \cdot \mathbf{u} d\mathbf{x} = 0, \tag{10}$$

and then proceed by discussing the discretization of each term, introducing $\mathbf{u}_h \in \boldsymbol{V}_F$ and $\mathbf{p}_h \in V_F$.
The spatial approximation of the first integral in (9) is straightforward, namely,

$$\int_{\kappa_F} \frac{\partial \mathbf{u}}{\partial t} d\mathbf{x} \approx \int_{\kappa_F} \frac{\partial \mathbf{u}_h}{\partial t} d\mathbf{x} = |\kappa_F| \frac{\partial \mathbf{u}_h}{\partial t}(\mathbf{x}_0^{\kappa_F}), \tag{11}$$

where $|\kappa_F|$ is the volume of the element κ_F and where a mid-point quadrature rule is employed. Next, being ν constant, we approximate the third term of (9) as follows

$$\int_{\kappa_F} \nabla \cdot (\nu \nabla \mathbf{u}) d\mathbf{x} = \int_{\partial \kappa_F} (\nu \nabla \mathbf{u}) \mathbf{n} ds \approx \sum_{\mathcal{F} \in \partial \kappa_F} \nu \nabla \mathbf{u}_{\mathcal{F}} \mathbf{n} |\mathcal{F}|,$$

where $\nabla \mathbf{u}_{\mathcal{F}} = \nabla \mathbf{u}(\mathbf{x}_{\mathcal{F}})$, being $\mathbf{x}_{\mathcal{F}}$ the face cell barycenter. Note that in the last step, we use a mid-point quadrature rule on the face $\mathcal{F}$. Now, if the face cell $\mathcal{F}$ is shared by two elements κ_F^+ and κ_F^-, we reconstruct linearly $\nabla \mathbf{u}_{\mathcal{F}} \mathbf{n}$. Concerning the convective term in (9), integrating by parts, we get:

$$\int_{\kappa_F} \nabla \cdot (\mathbf{u} \otimes \mathbf{u}) d\mathbf{x} = \int_{\partial \kappa_F} \mathbf{u} (\mathbf{u} \cdot \mathbf{n}) ds \approx \sum_{\mathcal{F} \in \partial \kappa_F} \mathbf{u}_{\mathcal{F}} (\mathbf{u}_{\mathcal{F}} \cdot \mathbf{n}) |\mathcal{F}|, \tag{12}$$

where $\mathbf{u}_{\mathcal{F}} = \mathbf{u}(\mathbf{x}_{\mathcal{F}})$, and where we applied a mid-point quadrature rule on the face $\mathcal{F}$. The value of the velocity at the face centre of $\mathcal{F}$ is often computed with a linear interpolation scheme, while the flux term is usually discretized with a linear upwind scheme. Finally, the pressure gradient term is discretized similarly, by observing that $\nabla p = \nabla \cdot (p\mathbf{I})$ and by applying the Gauss theorem. For the time discretization, we first divide the temporal interval $(0, T]$ into N subintervals, such that $T = N\Delta t$, setting $t^n = n\Delta t$, with $n = 0, \ldots, N$. We consider a backward differentiation formula of second order (BDF2) discretization scheme for (11), namely $\dfrac{\partial \mathbf{u}_h}{\partial t} \approx \dfrac{3\mathbf{u}_h^{n+1} - 4\mathbf{u}_h^n + \mathbf{u}_h^{n-1}}{2\Delta t}$. Finally, we remark that we compute at any time t^n the aeroacoustic sound source term as a post-process of the fluid solution $\mathbf{u}_h^n$, i.e., $\nabla \cdot \mathbf{T} \approx \nabla \cdot (\rho_0 \mathbf{u}_h^n \otimes \mathbf{u}_h^n)$, see (13) and also (12).

2.4 Discretization of the Lighthill's wave equation

We start by considering the variational formulation of the acoustic problem (8): *for* $t \in (0; T]$, *find* $\rho(\mathbf{x}, t) \in H^1(\Omega_A)$ *such that* $\forall w \in H^1(\Omega_A)$*:*

$$\left(\frac{\partial^2 \rho}{\partial t^2}, w \right)_{\Omega_A} + c_0^2 (\nabla \rho, \nabla w)_{\Omega_A} + c_0 \int_{\Gamma_O} \frac{\partial \rho}{\partial t} w \, ds = -(\nabla \cdot \mathbf{T}, \nabla w)_{\Omega_A}, \tag{13}$$

with initial conditions $\rho = \dfrac{\partial \rho}{\partial t} = 0$ in $\Omega_A \times \{0\}$, being $(\cdot, \cdot)_{\Omega_A}$ the L^2 product over the domain Ω_A. Remark that we integrated by parts the term $(\nabla \cdot \nabla \cdot \mathbf{T}, w)_{\Omega_A}$, by supposing that $\mathbf{T}$ is

null on the boundary of as it is done for instance in [26]. Next, we discretize problem (13) by means of the SEM as follows. We introduce a conforming decomposition $\mathcal{T}_A$ of the domain Ω_A made by hexahedral elements κ_A. We denote by $\widehat{\kappa}$ the reference element $[-1,1]^3$, and we suppose that for any mesh element $\kappa_A \in \mathcal{T}_A$ there exists a suitable trilinear invertible map $\boldsymbol{\theta}_{\kappa_A} : \widehat{\kappa} \to \kappa_A$ with positive Jacobian $\mathbf{J}_{\kappa_A}$. We define the characteristic mesh dimension as $h_A = \max_{\kappa_A \in \mathcal{T}_A} h_{\kappa_A}$, being h_{κ_A} the diameter of the element κ_A. Next, we introduce the finite-dimensional space: $V_A = \left\{ v \in C^0(\overline{\Omega}_A) \cap H^1(\Omega_A) : v|_{\kappa_A} \circ \boldsymbol{\theta}_{\kappa_A}^{-1} \in \mathbb{Q}_r(\widehat{\kappa}), \forall \kappa_A \in \mathcal{T}_A \right\}$, where $\mathbb{Q}_r(\widehat{\kappa})$ is the space of polynomials of degree less than or equal to $r \geq 1$ in each coordinate direction, and we denote by N_A the dimension of V_A. Next, for any $u, w \in V_A$, we introduce the following bilinear form by means of the Gauss-Legendre-Lobatto (GLL) quadrature rule:

$$(u,w)_{\kappa_A}^{NI} = \sum_{i,j,k=0}^{r} u(\boldsymbol{\theta}_{\kappa_A}(\boldsymbol{\xi}_{i,j,k}^{GLL}))w(\boldsymbol{\theta}_{\kappa_A}(\boldsymbol{\xi}_{i,j,k}^{GLL}))\omega_{i,j,k}^{GLL}|\det(\mathbf{J})| \approx (u,w)_{\kappa_A} \tag{14}$$

where $\boldsymbol{\xi}^{GLL}$ are the GLL quadrature nodes, and ω^{GLL} their corresponding weights, defined in $[-1,1]^3$ (cf. [36]) and NI stands for numerical integration. Moreover, we define

$$(u,w)_{\mathcal{T}_A}^{NI} = \sum_{\kappa_A \in \mathcal{T}_A} (u,w)_{\kappa_A}^{NI} \quad \forall\, u, w \in V_A.$$

The semi-discrete spectral element formulation of problem (13) with numerical integration (SEM-NI) reads: *for any time* $t \in (0;T]$ *find* $\rho_h \in V_A$ *such that:*

$$(\frac{\partial^2 \rho_h}{\partial t^2}, w_h)_{\mathcal{T}_A}^{NI} + c_0^2(\nabla \rho_h, \nabla w_h)_{\mathcal{T}_A}^{NI} + c_0 \int_{\Gamma_O} \frac{\partial \rho_h}{\partial t} w_h \, ds = -(\nabla \cdot \mathbf{T}, \nabla w_h)_{\mathcal{T}_A}^{QF} \quad \forall w_h \in V_A, \tag{15}$$

with $\rho_h = \dfrac{\partial \rho_h}{\partial t} = 0$ in $\Omega_A \times \{0\}$ and where $(\cdot,\cdot)_{\mathcal{T}_A}^{QF}$ refers to a suitable quadrature formula that will be described in Section 4.2. We recall that the term $\nabla \cdot \mathbf{T}$ is an external source that in our case is obtained from a numerical solution of problem (7) as described in Section 2.3. In the next section, we detail how to compute effectively the right-hand side of 15, i.e., how to approximate a field defined on the fluid mesh $\mathcal{T}_F$ with a field defined on the acoustic grid $\mathcal{T}_A$.

2.5 L^2–projection of the acoustic source

Let $q_F \in V_F$ be a function defined on the fluid grid $\mathcal{T}_F$ such that $q_F = \sum_{i=1}^{N_F} \widehat{q}_{F,i}\phi_{F,i}$, where $\left\{\phi_{F,i}\right\}_i^{N_F}$ is the set of N_F basis functions associated to V_F, and $\widehat{q}_{F,i}$ are the corresponding expansion coefficients. We define the L^2-projection of the field q_F into V_A as

$$q_A = \underset{q \in V_A}{\operatorname{argmin}} \left\| q_F - q \right\|_{L^2(\mathcal{T}_A)}. \tag{16}$$

Problem (16) is equivalent to the following: *find* $q_A \in V_A$ *s.t.*

$$(q_A, \phi_{A,i})_{\mathcal{T}_A} = (q_F, \phi_{A,i})_{\mathcal{T}_A} \quad \forall \phi_{A,i} \in V_A, \tag{17}$$

where $q_A \in V_A$ is a function defined on the acoustic grid $\mathcal{T}_A$ such that $q_A = \sum_{i=1}^{N_A} \widehat{q}_{A,i}\phi_{A,i}$, where $\left\{\phi_{A,i}\right\}_i^{N_A}$ is the set of N_A basis functions, and $\widehat{q}_{A,i}$ are the corresponding expansion coefficients. Motivated by the solution method used in Section 2.3 we address the case where

q_F is a piecewise constant over $\mathcal{T}_F$, namely $q_F \in V_F$. Then, problem (17) can be recast as follows:

$$\sum_{\kappa_A \in \mathcal{T}_A} (q_A, \phi_{A,i})_{\kappa_A} = \sum_{\kappa_A \in \mathcal{T}_A} (\sum_{\ell=1}^{N_F} \widehat{q}_{F,\ell} \phi_{F,\ell}, \phi_{A,i})_{\kappa_A} = \sum_{\kappa_A \in \mathcal{T}_A} \sum_{\ell=1}^{N_F} \widehat{q}_{F,\ell} (1, \phi_{A,i})_{\kappa_A \cap \kappa_{F,\ell}}, \tag{18}$$

where we have used that $\kappa_{F,\ell} = \text{supp}(\phi_{F,\ell})$. The discrete algebraic counterpart of (18) becomes

$$\mathbf{M}^{AA} \widehat{\mathbf{q}}_A = \mathbf{M}^{AF} \widehat{\mathbf{q}}_F, \tag{19}$$

where $\mathbf{M}^{AA} \in \mathbb{R}^{N_A \times N_A}$ is the acoustic mass matrix, i.e.,

$$\mathbf{M}^{AA}_{i,j} = \sum_{\kappa_A \in \mathcal{T}_A} (\phi_{A,j}, \phi_{A,i})_{\kappa_A}, \qquad i,j = 1, \dots, N_A, \tag{20}$$

while $\mathbf{M}^{AF} \in \mathbb{R}^{N_A \times N_F}$ is the coupling mass defined as

$$\mathbf{M}^{AF}_{i,\ell} = \sum_{\kappa_A \in \mathcal{T}_A} \int_{\kappa_A \cap \kappa_{F,\ell}} \phi_{A,i} \, \mathrm{d}\mathbf{x}, \qquad i = 1, \dots, N_A, \ \ell = 1, \dots, N_F. \tag{21}$$

The vector $\widehat{\mathbf{q}}_A$ in (19) collects all the expansion coefficients of the acoustic field q_A, while $\widehat{\mathbf{q}}_F$ collects all the expansion coefficients of the fluid field q_F.

3 Error analysis for the acoustic source

It is evident that the accuracy of the numerical solution ρ_h in (15) strongly depends on the approximation of the acoustic source, namely, $\nabla \cdot \mathbf{T}$. In our case the latter is obtained as a post-process of the numerical solution $\boldsymbol{u}_h$ of the flow problem. Quantifying the projection error between the acoustic and fluid grids is therefore of paramount importance.

However, before presenting the main result of the section we need to introduce some preliminary results.

Lemma 3.1 *(Interpolation error on GLL nodes). Given $f \in H^s(\Omega)$ for some $s \geq 1$, consider the Lagrangian interpolant $I_A^{GLL} f$ at the Gauss Legendre Lobatto nodes, where r denotes the polynomial degree of the interpolant function and h is the mesh size of $\mathcal{T}_h$ tessellation of Ω. Assuming h to be quasi uniform, we have that:*

$$\left\| f - I_A^{GLL} f \right\|_{L^2(\Omega)} \lesssim h^{\min(r+1,s)} \left(\frac{1}{r} \right)^s \left\| f \right\|_{H^s(\Omega)}. \tag{22}$$

For more details, see [6, Equation (5.4.3)].

Lemma 3.2 *(hp-inverse inequality) Assume now that $\kappa = \boldsymbol{\theta}_\kappa(\widehat{\kappa})$ is a hexahedral element s.t. $\kappa \subset \mathbb{R}^3$, where $\boldsymbol{\theta}_\kappa$ is a suitable trilinear map. Then we have that:*

$$\left\| \nabla v \right\|_{L^2(\kappa)} \lesssim \frac{r^2}{h_\kappa} \left\| v \right\|_{L^2(\kappa)}, \quad \forall v \circ \boldsymbol{\theta}_\kappa^{-1} \in \mathbb{Q}_r(\widehat{\kappa}), \tag{23}$$

where h_κ is $\text{diam}\,(\kappa)$.

For more details, see [40, Theorem 4.76]. Finally, we recall this Poincaré-Friedrich like inequality:

Lemma 3.3 *Given $u \in H^1(\kappa)$, where κ is an open bounded convex domain in $\mathbb{R}^d$ and $u \in L^2_0(\kappa) = \left\{ v \in L^2(\kappa) : \int_\kappa v = 0 \ d\mathbf{x} \right\}$ then we have that:*

$$\|u\|_{L^2(\kappa)} \lesssim \frac{\operatorname{diam}(\kappa)^{1+d/2}}{|\kappa|^{1/2}} \|\nabla u\|_{L^2(\kappa)}. \tag{24}$$

We refer the reader to [47, Corollary 3.4] and to [3, Remark 5.8] for further details.

Next, for the sake of the presentation, we consider the following setup: let $\Omega = \Omega_F = \Omega_A$ be a polygonal domain and let $\mathcal{T}_F$ and $\mathcal{T}_A$ be two nested grids of Ω as shown in Figure 2, namely for all elements $\kappa_A \in \mathcal{T}_A$ we assume that there exists a set of index $\mathcal{L}_{\kappa_A}$ such that $\kappa_A = \bigcup_{l \in \mathcal{L}_{\kappa_A}} \kappa_{F,l}$.

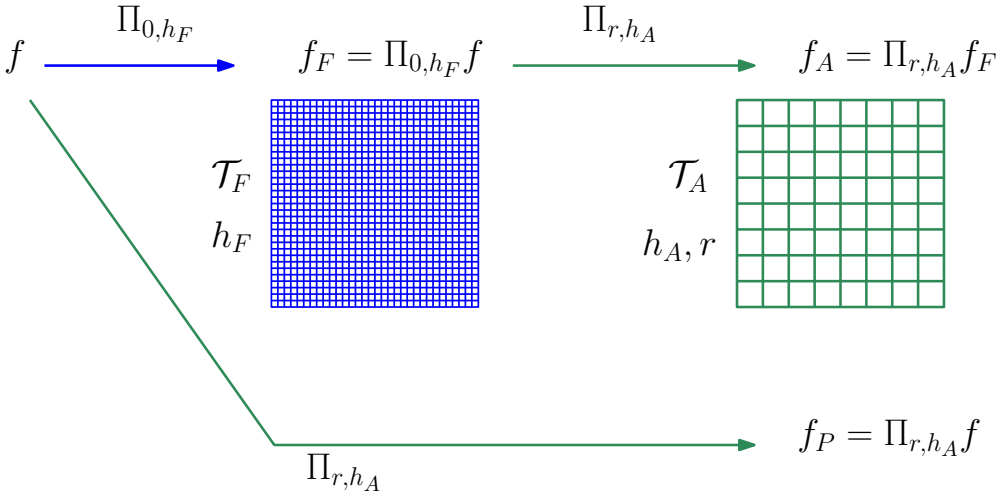

Figure 2: Schematic representation of the computational grids and the corresponding projection operators. For a given function $f \in L^2(\Omega)$, f_F is the projection $\Pi_{0,h_F} f$, f_A is the projection $\Pi_{r,h_A} f_F$ and f_P is the projection $\Pi_{r,h_A} f$. The computational grids $\mathcal{T}_A$ and $\mathcal{T}_F$ are assumed to be nested.

We now introduce the following projection operators: $\Pi_{0,h_F} : L^2(\Omega) \to V_F$ and $\Pi_{r,h_A} : L^2(\Omega) \to V_A$, and we define the following functions:

$$f_F = \Pi_{0,h_F} f, \tag{25}$$

that is the L^2 projection of $f \in L^2(\Omega)$ onto the space V_F,

$$f_P = \Pi_{r,h_A} f, \tag{26}$$

that is the L^2 projection of $f \in L^2(\Omega)$ onto the space V_A,

$$f_A = \Pi_{r,h_A} f_F, \tag{27}$$

that is the L^2 projection of $f_F \in V_F$ onto the space V_A, see Figure 2.
Now, we can state the following result.

Theorem 3.4 *(Approximation Theorem). Let $\mathcal{T}_A$ and $\mathcal{T}_F$ be two grids of the same computational domain $\Omega_F = \Omega_A = \Omega$ made by hexahedral elements, such that $\mathcal{T}_F$ is nested to $\mathcal{T}_A$, namely, for every element κ_F there exists κ_A such that $\kappa_F \subset \kappa_A$. Given $f \in H^s(\Omega)$ with*

$s \geq 1$, let $f_F = \Pi_{0,h_F} f$ be the projection of f onto the space V_F and let $f_A = \Pi_{r,h_A} f_F$, namely the projection of f_F onto the space V_A. Then, it holds:

$$\left\| f - f_A \right\|_{L^2(\Omega)} \lesssim h_A^{\min(r+1,s)} \left(\frac{1}{r}\right)^s \left\| f \right\|_{H^s(\Omega)} + \frac{h_F^2}{h_A} r^2 \left\| f \right\|_{H^s(\Omega)}. \tag{28}$$

Proof. Let $f_P = \Pi_{r,h_A} f$, see for instance Figure 2. By triangular inequality we have that

$$\left\| f - f_A \right\|_{L^2(\Omega)} \leq \left\| f - f_P \right\|_{L^2(\Omega)} + \left\| f_P - f_A \right\|_{L^2(\Omega)}. \tag{29}$$

The first term on the right hand side can be estimated by employing Lemma 3.1, i.e.:

$$\left\| f - f_P \right\|_{L^2(\Omega)} = \min_{\varphi \in V_A} \left\| f - \varphi \right\|_{L^2(\Omega)} \lesssim \left\| f - I_A^{GLL} \right\|_{L^2(\Omega)} \lesssim h_A^{\min(r+1,s)} \left(\frac{1}{r}\right)^s \left\| f^{(s)} \right\|_{H^s(\Omega)}. \tag{30}$$

Next, we observe that by definition of the L^2-projection we get

$$(f_A, \phi)_{L^2(\Omega)} = (f_F, \phi)_{L^2(\Omega)} \quad \forall \phi \in V_A, \tag{31}$$

$$(f_P, \phi)_{L^2(\Omega)} = (f, \phi)_{L^2(\Omega)} \quad \forall \phi \in V_A. \tag{32}$$

Then, by subtracting (31) to (32), we obtain

$$(f_P - f_A, \phi)_{L^2(\Omega)} = (f - f_F, \phi)_{L^2(\Omega)}, \quad \forall \phi \in V_A.$$

Furthermore, since $f_P - f_A \in V_A$, we can write

$$\left\| f_P - f_A \right\|^2_{L^2(\Omega)} = \int_\Omega (f - f_F)(f_P - f_A) \, \mathrm{d}\mathbf{x} = \sum_{\kappa_F} \int_{\kappa_F} (f - f_F)(f_P - f_A) \, \mathrm{d}\mathbf{x}.$$

and notice that

$$(f - f_F, \varphi)_{L^2(\kappa_F)} = 0 \quad \forall \varphi \in \mathbb{P}^0(\kappa_F),$$

where $\mathbb{P}^0(\kappa_F)$ is the space of the constant functions over κ_F. By taking $\varphi = \Pi_{0,h_F}(f_P - f_A)$ in the above equation yields to

$$\begin{aligned}
\sum_{\kappa_F} \int_{\kappa_F} (f - f_F)(f_P - f_A) \, \mathrm{d}\mathbf{x} &= \sum_{\kappa_F} \int_{\kappa_F} (f - f_F)(f_P - f_A - \Pi_{0,h_F}(f_P - f_A)) \, \mathrm{d}\mathbf{x}. \\
&\lesssim \sum_{\kappa_F} \left\| f - f_F \right\|_{L^2(\kappa_F)} \left\| f_P - f_A - \Pi_{0,h_F}(f_P - f_A) \right\|_{L^2(\kappa_F)} \\
&\lesssim h_F^2 \sum_{\kappa_F} \left\| \nabla f \right\|_{L^2(\kappa_F)} \left\| \nabla (f_P - f_A) \right\|_{L^2(\kappa_F)},
\end{aligned} \tag{33}$$

where in the last inequality we employ Lemma 3.3. By linearity of the integral, noticing that by hypothesis $\kappa_F \subset \kappa_A$ and using that $\left\| \nabla f \right\|_{L^2(\kappa_F)} \leq \left\| \nabla f \right\|_{L^2(\kappa_A)}$ we obtain

$$\begin{aligned}
\sum_{\kappa_F} h_F^2 \left\| \nabla f \right\|_{L^2(\kappa_F)} \left\| \nabla (f_P - f_A) \right\|_{L^2(\kappa_F)} &\lesssim \sum_{\kappa_A} h_F^2 \left\| \nabla f \right\|_{L^2(\kappa_A)} \left\| \nabla (f_P - f_A) \right\|_{L^2(\kappa_A)} \\
&\lesssim \sum_{\kappa_A} \frac{h_F^2 r^2}{h_A} \left\| \nabla f \right\|_{L^2(\kappa_A)} \left\| f_P - f_A \right\|_{L^2(\kappa_A)} \\
&\lesssim \frac{h_F^2 r^2}{h_A} \left\| \nabla f \right\|_{L^2(\Omega)} \left\| f_P - f_A \right\|_{L^2(\Omega)},
\end{aligned}$$

where in the last step we used the inverse inequality of Lemma 3.2. Finally, we get

$$\left\| f_P - f_A \right\|^2_{L^2(\Omega)} \lesssim \frac{h_F^2 r^2}{h_A} \left\| \nabla f \right\|_{L^2(\Omega)} \left\| f_P - f_A \right\|_{L^2(\Omega)},$$

or equivalently,

$$\left\| f_P - f_A \right\|_{L^2(\Omega)} \lesssim \frac{h_F^2 r^2}{h_A} \left\| \nabla f \right\|_{L^2(\Omega)} \tag{34}$$

and that concludes the proof. □

4 Implementation aspects

An accurate solution of the projection problem (18) requires computing the intersection between the elements $\kappa_A \in \mathcal{T}_A$ and $\kappa_F \in \mathcal{T}_F$. This operation is in general very expensive, but in many applications, it is crucial to compute it accurately in order to have reliable solutions. In this section, we present our strategy to compute the intersection between two elements κ_A and κ_F and show that it is robust and scalable. We recall that the intersection $\kappa = \kappa_A \cap \kappa_F$ is in general a polyhedron in the three-dimensional space. Moreover, we describe the employed quadrature-free algorithm to compute the integral of polynomials functions over κ, cf. Equation (21).

4.1 Intersection algorithm

The benefits of computing explicitly the intersection elements when projecting have been already explored in the context of low-order finite elements for aeroacoustics on tetrahedral meshes, see for instance [39]. The new grid obtained after the intersection is nested both with respect to the fluid grid and with respect to the acoustic grid, hence we can apply the analysis of Section 3. Here, we propose a geometrical algorithm for computing the intersections between generic polyhedral grids. In particular, we consider a polyhedral tessellation $\mathcal{T}_F$ for the fluid domain Ω_F, while a hexahedral tessellation $\mathcal{T}_A$ for the acoustic domain Ω_A, see for instance Figure 3a. This choice is inherited from the numerical scheme that we apply to the aeroacoustic problem (see Section 2.3- 2.4), even if the proposed algorithm is valid for generic polyhedral grids. Depending on the characteristic wave-length of the problem and on the numerical schemes considered, we assume that the number of fluid elements κ_F is greater than the number of acoustic ones κ_A and that the elements are all convex polyhedra. Considering polyhedra elements allows us to use the Separating Axis Theorem (SAT) for detecting if two elements have non-empty intersection. The main idea of the SAT is that, if two elements have empty intersection, then there exists a plane that separates them. Only a few directions depending on the normals to the faces of the elements and the edge elements have to be checked. A detailed description of the SAT algorithm can be found in [12, Chapter 8]. Before presenting the algorithm for computing the intersections between κ_A and κ_F we introduce some definitions and notations.

Definition 4.1 *(Cartesian Bounding Box) Given a polyhedral element $\kappa \subset \mathbb{R}^3$, we denote with $\mathbf{v}_i = (x_i, y_i, z_i)$ with $i = 1, \dots, n_v$ the n_v vertices of κ. We indicate with $\mathcal{B}(\kappa)$ his Cartesian bounding box:*

$$\mathcal{B}(\kappa) = \Pi_{\alpha \in \{x,y,z\}} [\alpha_{min}, \alpha_{max}], \tag{35}$$

where $\alpha_{min} = \min_{i=1,\dots,n_v} \alpha_i$, $\alpha_{max} = \max_{i=1,\dots,n_v} \alpha_i$.

For any element $\kappa_A \in \mathcal{T}_A$, we define:

- the set $\mathcal{K}_A$ collecting all the fluid elements κ_F whose bounding box $\mathcal{B}(\kappa_F)$ intersects the bounding box $\mathcal{B}(\kappa_A)$, i.e., $\mathcal{B}(\kappa_F) \cap \mathcal{B}(\kappa_A) \neq \emptyset$;
- the set $\mathcal{C}_A$ collecting all the fluid elements κ_F whose bounding box $\mathcal{B}(\kappa_F)$ is strictly contained inside κ_A, i.e. $\mathcal{B}(\kappa_F) \subset \kappa_A$;
- the set $\mathcal{I}_A$ collecting all the fluid elements κ_F that have to be explicitly intersected with κ_A.

We remark that the cardinality of $\mathcal{K}_A$ is strictly greater than the cardinality of $\mathcal{C}_A \cup \mathcal{I}_A$. Algorithm 1 computes the intersections between $\mathcal{T}_A$ and $\mathcal{T}_F$ proceeding as follows: for any

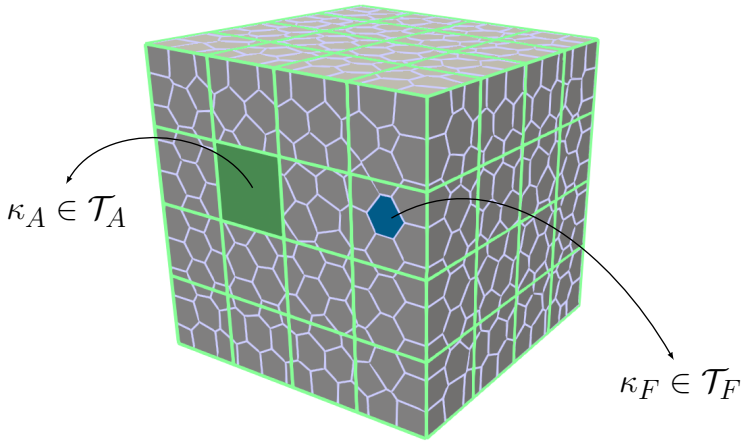

(a) Example of acoustic $\mathcal{T}_A$ and fluid $\mathcal{T}_F$ tessellations made of hexahedral and polyhedral elements, respectively, for the domain $\Omega = \Omega_A = \Omega_F$.

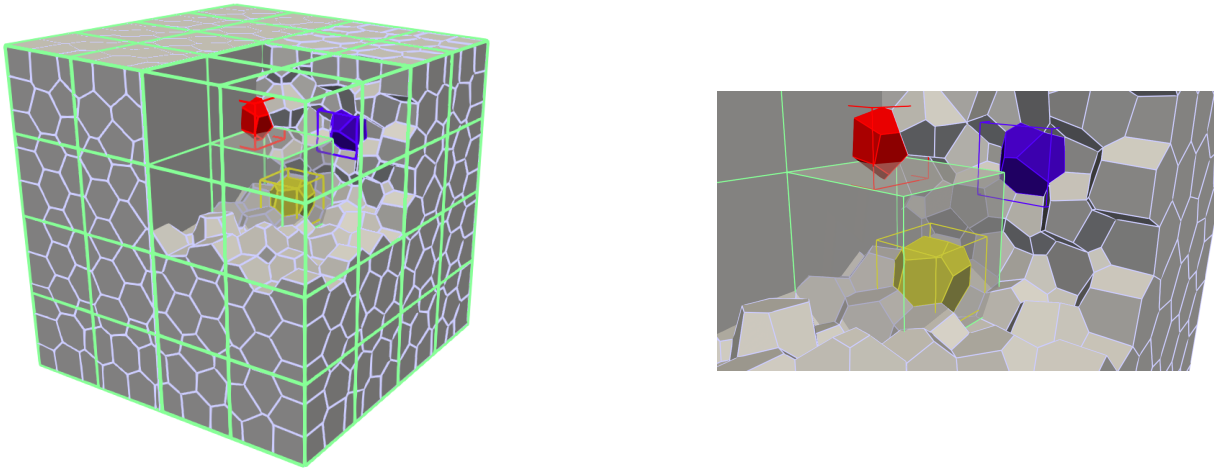

(b) *Bounding Box search.* Left, overview on the whole domain. Right, zoom on a selected acoustic element κ_A. At this stage, all the bounding box of the fluid elements intersecting $\mathcal{B}(\kappa_A)$ are selected and collected in the set $\mathcal{K}_A$. We show some of the selected fluid elements (yellow •, red • and blue •) and their respective bounding box.

Figure 3: Schematic representation of Algorithm 1. (•) Acoustic element κ_A. (•) Example of a fluid element $\kappa_F \in \mathcal{I}_A$. (•) Example of a fluid element $\kappa_F \in \mathcal{K}_A$ but not intersecting with the selected element κ_A. (•) Example of a fluid element $\kappa_F \in \mathcal{C}_A$.

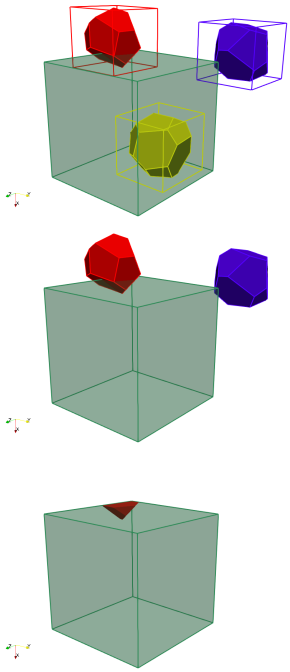

(a) *Bounding Box selection.* At this stage, we check if the bounding box of a fluid element is contained inside κ_A. For example, the yellow (•) fluid element is contained in κ_A, and hence it is added to $\mathcal{C}$.

(b) *Separating Axis Theorem selection.* At this stage, we check if the fluid elements in $\mathcal{K}_A \setminus \mathcal{C}_A$ are intersecting with κ_A. We see that the red element (•) is intersecting, and hence it is pushed in $\mathcal{I}$. The blue element (•) is not intersecting, so it is discarded.

(c) *Intersection computation.* The intersection is explicitly computed only for the red element (•). A new object is obtained, which is then stored and used for the projection computation.

Figure 4: Schematic representation of Algorithm 1. (•) Acoustic element κ_A. (•) Example of a fluid element $\kappa_F \in \mathcal{I}_A$. (•) Example of a fluid element $\kappa_F \in \mathcal{K}_A$ but not intersecting with the selected element κ_A. (•) Example of a fluid element $\kappa_F \in \mathcal{C}_A$.

element $\kappa_A \in \mathcal{T}_A$,

1. *Bounding Box search*: search over the intersecting bounding boxes of the fluid elements $\mathcal{B}(\kappa_F)$ and the bounding box $\mathcal{B}(\kappa_A)$ of the acoustic element κ_A. If the intersection is not empty, the element κ_F is added to the set $\mathcal{K}_A$, see Figure 3b.
2. *Bounding Box selection*: map the vertices of $\mathcal{B}(\kappa_F)$ via a Newton-Raphson algorithm by employing the trilinear map $\boldsymbol{\theta}_{\kappa_A}$. If all the vertices are inside the reference element $\widehat{\kappa}_A$, then κ_F is added to $\mathcal{C}_A$, see Figure 4a.
3. *Separating Axis Theorem selection*: apply the SAT collision detection algorithm in order to understand if the intersections have to be computed. In fact, there might be fluid elements in $\mathcal{K}_A$ that are not effectively intersecting κ_A, see for instance Figure 4b. The intersecting elements are added to $\mathcal{I}_A$.
4. *Intersection computation*: compute explicitly the intersection between the fluid elements in $\mathcal{I}_A$ and the acoustic element κ_A, cf. Figure 4c.

We remark that Step 2. of the algorithm is justified by the assumption that fluid elements are much smaller then the acoustic ones. The final intersection (Step 4.) is computed by employing the Computational Geometry Algorithms Library (CGAL) [44], and it is based on the Nef implementation [20] that allows performing Boolean operations between solids.

4.2 A quadrature-free method for integral evaluation

In this section, we explain how to compute numerically the integrals defined on the right-hand side of (18). In the aeroacoustic solver this technique is used for computing the right-hand side of (15). We remark that if in V_A we consider only linear polynomials in

Algorithm 1 Algorithm to compute the intersection $\mathcal{T}_A \cap \mathcal{T}_F$ between the grids $\mathcal{T}_A$ and $\mathcal{T}_F$.

$[\mathcal{T}_A \cap \mathcal{T}_F]$ = `compute intersection`$(\mathcal{T}_A, \mathcal{T}_F)$
for $\kappa_A \in \mathcal{T}_A$ **do**
  Compute $\mathcal{B}(\kappa_A)$.
  for $\kappa_F \in \mathcal{T}_F$ **do**
    Compute $\mathcal{B}(\kappa_F)$.
    if $\mathcal{B}(\kappa_A) \cap \mathcal{B}(\kappa_F)$ **then**
      Add κ_F in $\mathcal{K}_A$.
      if $\mathcal{B}(\kappa_F) \subset \kappa_A$ **then**
        $\kappa_F \cap \kappa_A = \kappa_F$ and $\kappa_F \in \mathcal{C}_A$.
      end if
      if $\kappa_A \cap \kappa_F$ **then**
        Add κ_F in $\mathcal{I}_A$.
      else
        Elements are not intersecting.
      end if
    end if
  end for
  for ($\kappa_F \in \mathcal{I}_A$) **do**
    Compute intersection $(\kappa_A \cap \kappa_F)$ with CGAL.
  end for
end for

each space direction, i.e., $r = 1$, and if the maps $\boldsymbol{\theta}_{\kappa_A}$ are linear for any $\kappa_A \in \mathcal{T}_A$, then it is convenient to use a mid-point quadrature method. In this case, (19) becomes

$$\sum_{\kappa_A \in \mathcal{T}_A} (q_A^\pi, \phi_{A,i})_{\kappa_A} = \sum_{\kappa_A \in \mathcal{T}_A} \sum_{\ell=1}^{N_F} \widehat{q}_{F,\ell} (1, \phi_{A,i})_{\kappa_A \cap \kappa_{F,\ell}} = \sum_{\kappa_A \in \mathcal{T}_A} \sum_{\ell=1}^{N_F} \widehat{q}_{F,\ell} \phi_{A,i}(\boldsymbol{x}_b) |\kappa_A \cap \kappa_{F,\ell}|, \tag{36}$$

where $\boldsymbol{x}_b$ is the barycentre of the intersection element $\kappa_A \cap \kappa_{F,\ell}$, and $|\kappa_A \cap \kappa_{F,\ell}|$ is the volume of the intersection. This is exactly the cut-volume cell-based interpolation that has been proposed in [39]. However, considering higher-order polynomials, i.e., $r > 1$ in V_A, or generic trilinear maps, leads to inexact quadrature integration that deteriorates the quality of the projection. For this reason, we look for a quadrature formula that is able to integrate high-order polynomials on generic polyhedral elements (intersection of fluid and acoustic elements). When integrating polynomials over a polyhedral domain, one of the most popular choices is to sub-tessellate the polyhedral domain and then apply therein a standard quadrature formula over the tetrahedral mesh. This is in general computationally expensive. For that reason we employed a Laserre-like integration [8], that has already been successfully applied in the context of discontinuous Galerkin methods, see for instance [5]. The employed quadrature formula is able to integrate exactly homogeneous functions over general polyhedra κ. We report here for completeness the main feature of the quadrature method, and refer to [5] for further details. Let the polyhedron $\kappa \subset \mathbb{R}^3$ be a closed polytope, whose boundary $\partial\kappa$ is defined by m faces $\mathcal{F}_i \in \mathbb{R}^2$, with $i = 1, \dots, m$. To each face $\mathcal{F}_i$ we associate a normal vector $\mathbf{n}_i$. Also, each face $\mathcal{F}_i$ lies on a hyperplane $\mathcal{H}_i$, and hence to each face $\mathcal{F}_i$ we associate a scalar b_i such that $\forall \mathbf{x} \in \mathcal{H}_i$ we have that $\mathbf{n}_i \cdot \mathbf{x} = b_i$. Moreover, we split the polyhedron boundary as the union of m faces, i.e., $\partial\kappa = \bigcup_i^m \mathcal{F}_i$, and the boundary

of each face $\mathcal{F}_i$ as the union of m_i edges, i.e., $\partial\mathcal{F}_i = \bigcup_j^{m_i} \mathcal{F}_{ij}$. Finally, the m_{ij} vertices of each edge $\mathcal{F}_{ij}$ are denoted by $\partial\mathcal{F}_{ij} = \bigcup_k^{m_{ij}} \mathcal{F}_{ijk}$. Let g to be homogeneous of degree $q > 0$, namely,

$$qg(\mathbf{x}) = \nabla g(\mathbf{x}) \cdot \mathbf{x} \quad \forall \mathbf{x} \in \kappa, \tag{37}$$

and recall the generalized Stokes' theorem, see [43]:

$$\int_\kappa (\nabla \cdot \mathbf{V}(\mathbf{x}))g(\mathbf{x})\mathrm{d}\mathbf{x} + \int_\kappa \nabla g(\mathbf{x}) \cdot \mathbf{V}(\mathbf{x})\mathrm{d}\mathbf{x} = \int_{\partial\kappa} \mathbf{V}(\mathbf{x}) \cdot \mathbf{n} g(\mathbf{x}) d\sigma, \tag{38}$$

where $\mathbf{V} : \kappa \to \mathbb{R}^3$ is a generic vector field. By selecting $\mathbf{V}(\mathbf{x}) = \mathbf{x}$, and by applying (37) we have

$$\int_\kappa g(\mathbf{x})\mathrm{d}\mathbf{x} = \frac{1}{3+q} \int_{\partial\kappa} \mathbf{x} \cdot \mathbf{n} g(\mathbf{x}) d\sigma = \frac{1}{3+q} \sum_{i=1}^{m} b_i \int_{\mathcal{F}_i} g(\mathbf{x}) d\sigma. \tag{39}$$

Next, by applying recursively integration by parts on (39), we obtain the following quadrature formula for computing the integral of a homogeneous function over a polyhedron κ:

$$\begin{aligned} \int_\kappa g(\mathbf{x})\mathrm{d}\mathbf{x} &= \frac{1}{q+3} \sum_{i=1}^{m} \frac{b_i}{2+q} \left(\sum_{j=1}^{m_i} d_{ij} \int_{\mathcal{F}_{ij}} g(\mathbf{x}) d\nu + \int_{\mathcal{F}_i} \mathbf{x}_{0,i} \cdot \nabla g(\mathbf{x}) d\sigma \right), \\ \int_{\mathcal{F}_{ij}} g(\mathbf{x}) d\nu &= \frac{1}{1+q} \left(\sum_{k=1}^{m_{ij}} d_{ijk} \int_{\mathcal{F}_{ijk}} g(\mathbf{x}) d\xi + \int_{\mathcal{F}_{ij}} \mathbf{x}_{0,ij} \cdot \nabla g(\mathbf{x}) d\nu \right), \end{aligned} \tag{40}$$

where d_{ij} is the Euclidean distance between the arbitrary point $\mathbf{x}_{0,i}$ and the edge $\mathcal{F}_{ij}$ and d_{ijk} is the Euclidean distance between the arbitrary point $\mathbf{x}_{0,ij} \in \mathcal{F}_{ij}$ and the vertex $\mathcal{F}_{ijk}$. We now apply the quadrature free rule described by Equation (40) to (18) since the integrated function is a polynomial, namely, it is a homogeneous function of degree r. Moreover, since we are employing spectral element methods, we usually integrate over a family of monomials. To speed up the whole algorithm, the integrated monomials over κ are stored and reused upon need. For further details on the implementation, we refer to Algorithm 2 in [5].

5 Computational aspect of the intersection algorithm

In this section, we investigate some computational aspects of the algorithm presented in Section 4.1. First, we verify the intersection algorithm in terms of accuracy and scalability. Then, we use Algorithm 1 together with the quadrature-free method in Section 4.2 to compute integrals of polynomials over the domain Ω.

To check the accuracy of the proposed intersection algorithm we consider the following mesh configurations. In the first test, we set $\Omega = \Omega_F = \Omega_A = (-2, 2) \times (-2, 2) \times (-0.05, 0.05)$ and define the acoustic grid $\mathcal{T}_A^1$ (resp. fluid grid $\mathcal{T}_F^1$) by extruding in the vertical direction distorted quadrilaterals (resp. polygons), cf. Figure 5. The acoustic grid has 64 elements and the original Cartesian mesh size was $h_A = 0.5$, while the fluid grid has 109 elements and $h_F = 0.5$. In the second test, we consider $\Omega = \Omega_F = \Omega_A = (-0.5, 0.5)^3$ and use a Cartesian grid $\mathcal{T}_A^2$ with 64 elements and $h_A = 0.25$ in Ω_A, while a Voronoi polyhedral grid $\mathcal{T}_F^2$ with 1000 elements and $h_F = 0.1$ in Ω_F, see Figure 6. The computed intersections are shown in Figures 5 and 6 (right). To have a quality check of the performed algorithm we color the resulting grid $\mathcal{T}_A^1 \cap \mathcal{T}_F^1$ in the following way. All the intersections between

$E_{rel}(f) = \left\lvert \left(\int_\Omega f d\mathbf{x} - \int_\mathcal{T} f d\mathbf{x} \right) \Big/ \left(\int_\Omega f d\mathbf{x} \right) \right\rvert$	$\mathcal{T}_A^1$	$\mathcal{T}_F^1$	$\mathcal{T}_A^1 \cap \mathcal{T}_F^1$
$E_{rel}(1)$	5.551×10^{-16}	5.551×10^{-16}	5.551×10^{-16}
$E_{rel}(x^2y^2)$	6.661×10^{-16}	4.441×10^{-16}	1.11×10^{-16}
$E_{rel}(x^4y^4)$	8.882×10^{-16}	4.441×10^{-16}	2.22×10^{-16}

Table 1: Computed error for different meshes: acoustic grid $\mathcal{T}_A^1$, fluid grid $\mathcal{T}_F^1$ and their intersection $\mathcal{T}_A^1 \cap \mathcal{T}_F^1$. Here, $\Omega = (-2, 2) \times (-2, 2) \times (-0.05, 0.05)$.

$E_{rel}(f) = \left\lvert \left(\int_\Omega f d\mathbf{x} - \int_\mathcal{T} f d\mathbf{x} \right) \Big/ \left(\int_\Omega f d\mathbf{x} \right) \right\rvert$	$\mathcal{T}_A^2$	$\mathcal{T}_F^2$	$\mathcal{T}_A^2 \cap \mathcal{T}_F^2$
$E_{rel}(1)$	0	4.441×10^{-16}	0
$E_{rel}(x^2y^2z^2)$	0	2.22×10^{-16}	0
$E_{rel}(x^4y^4z^4)$	4.441×10^{-16}	1.11×10^{-15}	0

Table 2: Computed error for different meshes $\mathcal{T}$: acoustic grid $\mathcal{T}_A^2$, fluid grid $\mathcal{T}_F^2$ and their intersection $\mathcal{T}_A^2 \cap \mathcal{T}_F^2$. Here, $\Omega = (-0.5, 0.5)^3$.

elements in $\mathcal{T}_F^1$ and a single element in $\mathcal{T}_A^1$ have the same color. It is possible to notice that even small elements are intersected properly by the proposed intersection algorithm, cf. Figures 5 and 6 (right). To show the accuracy of the proposed intersection algorithm, we consider the following verification test that computes the integral of polynomial functions over the intersection grid $\mathcal{T}_A \cap \mathcal{T}_F$. In Tables 1 and 2 we report the relative errors $E_{rel}(f) = \left\lvert \left(\int_\Omega f d\mathbf{x} - \int_\mathcal{T} f d\mathbf{x} \right) \Big/ \left(\int_\Omega f d\mathbf{x} \right) \right\rvert$, computed by employing the quadrature free method in Section 4.2, by varying the mesh $\mathcal{T}$ of the domain Ω. Here, ϕ is a generic monomial function. Since the quadrature-free algorithm is exact for homogeneous functions, from the results it is possible to conclude that the intersection computation does not introduce any additional error.

To assess the scalability of the algorithm we consider $\Omega = \Omega_F = \Omega_A = (-0.5, 0.5)^3$. We tessellate the domain Ω_A (resp. Ω_F) with a grid made by 32^3 (resp. 65^3) elements. The total number of computed intersections is 884736, with $\sum_{\kappa_A \in \mathcal{T}_A} \text{card}(\mathcal{C}_A) = 39304$ and $\sum_{\kappa_A \in \mathcal{T}_A} \text{card}(\mathcal{I}_A) = 845432$, see Section 4.1, that is where most of the computational time is spent by the algorithm concerns the evaluation of actual intersections, i.e., lines 17-19 of Algorithm 1.

We perform a strong scalability test on the G100 cluster located at Cineca, by keeping the same computational grids while varying the number of available cores. From Figure 7 it is possible to notice that the algorithm scales well up to 128 cores. Then, since the partitioning of the acoustic mesh is independent of the underlying fluid grid, the number of intersecting elements for larger decompositions might vary largely between the processors, leading to unbalance in the intersection computations. To verify this, we design a larger test where an acoustic Cartesian grid with 64^3 elements and a fluid grid with 65^3 elements are considered.

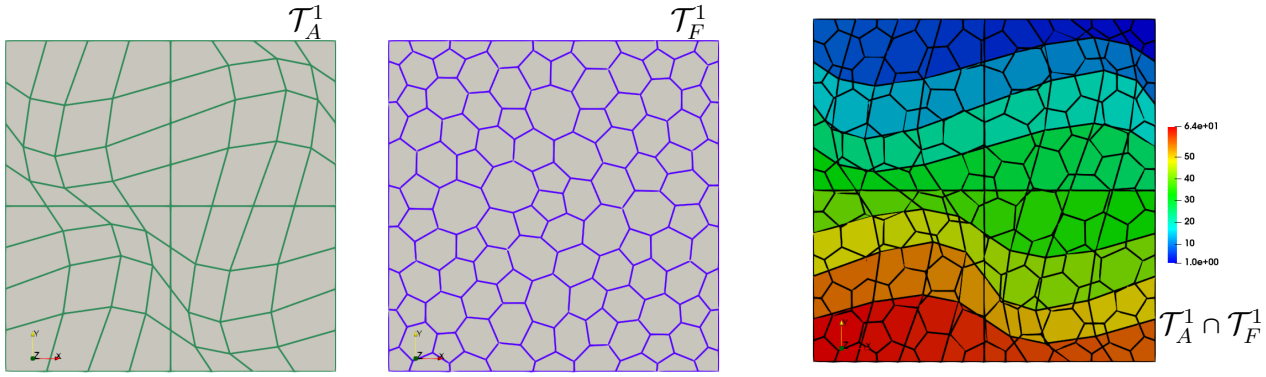

Figure 5: Two-dimensional view of Intersection between $\mathcal{T}_A^1$ (left) and $\mathcal{T}_F^1$ (center). The considered computational grids are first generated in two dimensions and then extruded, with only one element in the vertical direction. All the intersections between elements in $\mathcal{T}_F^1$ and a single element in $\mathcal{T}_A^1$ have the same color.

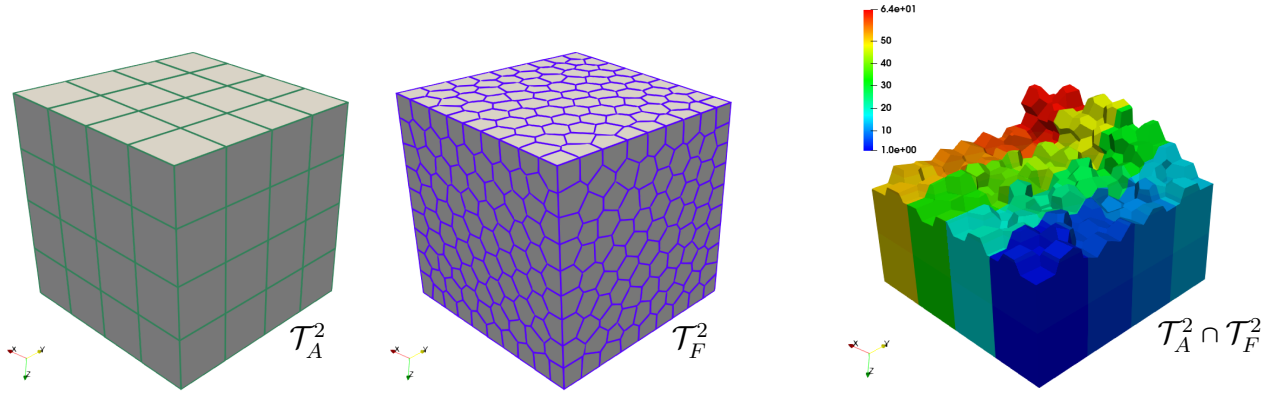

Figure 6: Intersection between $\mathcal{T}_A^2$ (left) and $\mathcal{T}_F^2$ (center). The fluid grid is made of polyhedral elements, while the acoustic grid is made of hexahedral elements. All the intersections between elements in $\mathcal{T}_F^2$ and a single element in $\mathcal{T}_A^2$ have the same color.

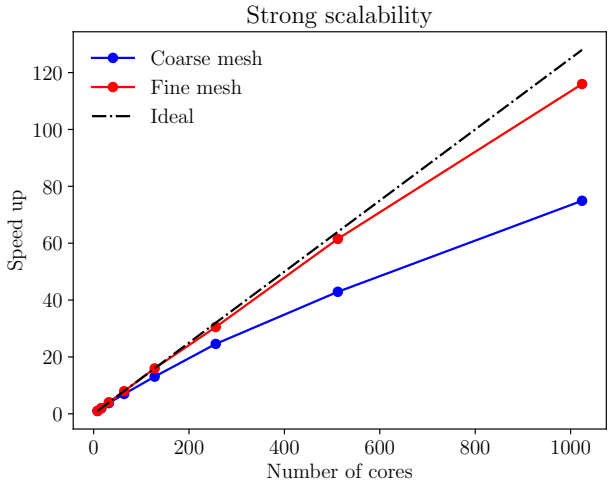

Figure 7: Scalability test. The speed-up is computed with respect to the test performed on 8 cores. The coarse mesh has 884736 intersections, while the fine mesh has 7077888 intersections.

The total number of computed intersections is $\sum_{\kappa_A \in \mathcal{T}_A} \mathrm{card}(\mathcal{I}_A) = 7077888$. On this latter test, where more elements are employed, the balance of the intersection is good and the scalability is almost ideal.

6 Convergence results for the L^2-projection method

In this section, we inquire about the convergence properties of the developed projection method. In particular, we verify the theoretical estimate in Theorem 3.4 for the approximation error $\|f - f_A\|_{L^2(\Omega)}$ and compare our approach with the one presented in [39].

6.1 Verification and validation test cases

We consider a cubic domain $\Omega = \Omega_A = \Omega_F = (-0.5, 0.5)^3$ and two Cartesian nested tessellation $\mathcal{T}_A$ and $\mathcal{T}_F$, being the acoustic mesh size h_A a multiple of fluid one h_F. Next, we consider $f = \cos(2\pi x)\cos(2\pi y)\cos(\pi z)$ and compute $E_A = \|f - f_A\|_{L^2(\Omega)}$, where f_A is the projection defined as in Figure 2. In Figure 8 we report the projection error E_A, by varying h_F for fixed values of h_A and of the polynomial degree r. It is clear that the error E_A saturates as we refine h_F. Indeed, by triangle inequality, we observe that

$$E_A \leq \|f - f_P\|_{L^2(\Omega)} + \|f_P - f_A\|_{L^2(\Omega)}, \tag{41}$$

and that $\|f - f_P\|_{L^2(\Omega)}$ is the leading term of the error independent of h_F. This is confirmed by the plots reported in Figure 9 where we show the trend of the error $\|f_P - f_A\|_{L^2(\Omega)}$ as a function of h_F. The latter is proportional to h_F^2 as predicted by (34). On the other hand, the error $\|f - f_P\|_{L^2(\Omega)}$ remains constant, cf. (30). Moreover, we notice that increasing the polynomial degree r, keeping fixed h_A, reduces the saturation value reached by the error $\|f - f_A\|_{L^2(\Omega)}$. Finally, in Figure 10 (left), we plot the error $\|f - f_P\|_{L^2(\Omega)}$ versus the mesh size h_A while in Figure 10 (right) the same quantity is shown as a function of r. The expected convergence rate given by estimate (30) is confirmed by the numerical results.

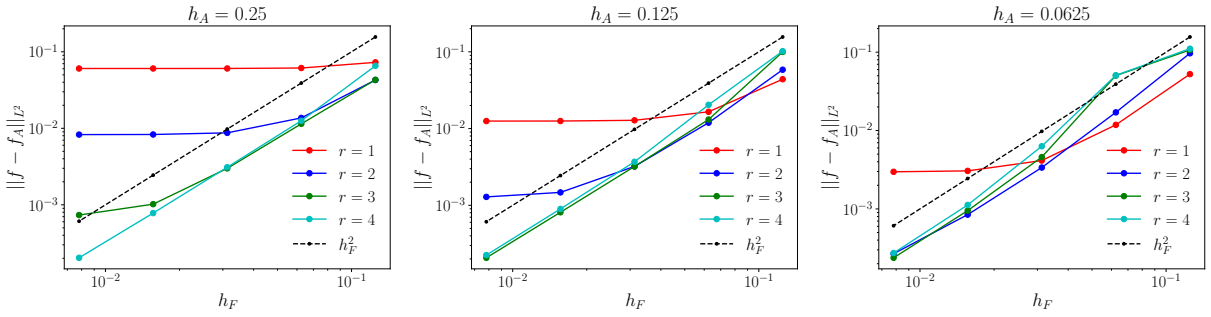

Figure 8: Computed errors $\|f - f_A\|_{L^2(\Omega)}$ versus h_F, for different polynomial degrees $r = 1, 2, 3, 4$ and different choices of $h_A = 0.25, 0.125, 0.0625$ (loglogscale).

We provide the following rule of thumb to decide how to relate the acoustic and fluid grid in terms of mesh sizes h_A, h_F, and polynomial degree r. Lower projection errors would be generally obtained if both grids have a similar number of degrees of freedom. As seen from estimate (28), the approximation error E_A is lower employing for the acoustic problem a low order polynomial degree and a spatial resolution comparable to the fluid grid, namely

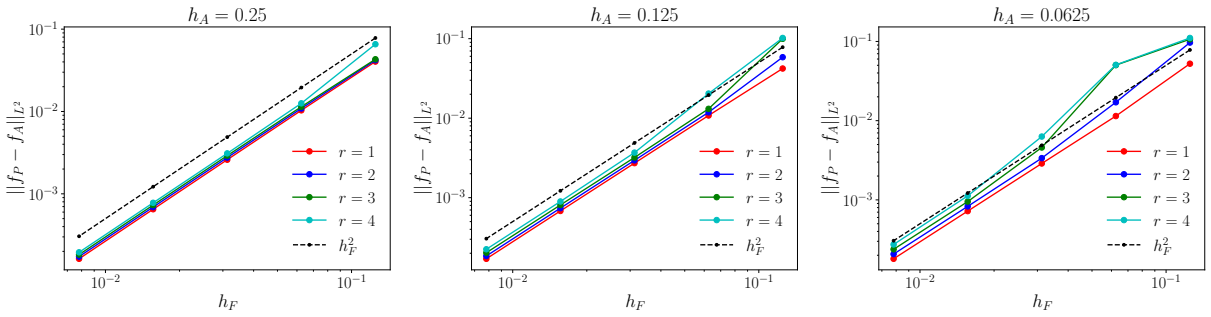

Figure 9: Computed errors $\|f_P - f_A\|_{L^2(\Omega)}$ versus h_F, for different polynomial degrees $r = 1, 2, 3, 4$ and different choices of $h_A = 0.25, 0.125, 0.0625$ (loglogscale).

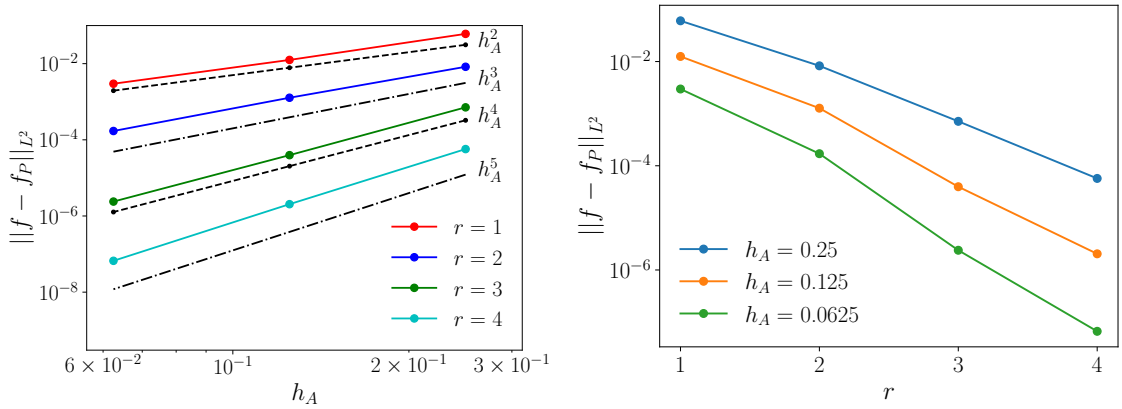

Figure 10: Computed errors $\|f - f_P\|_{L^2(\Omega)}$ versus h_A (left) and r (right), for different choices of $r = 1, 2, 3, 4$ and $h_A = 0.25, 0.125, 0.0625$ (loglogscale).

$h_F \approx h_A$. However, this choice deteriorates the convergence error estimates provided by the Strang Lemma for the SEM-NI method, see e.g., [36, Lemma 10.1]. The numerical tests presented above show that the dependency on the polynomial degree is not so severe as stated in eq. (28), encouraging the use of high-order basis functions.

Next, as a further validation example we compute the error $\|f - f_A\|_{L^2(\Omega)}$, where $f = \cos(\pi x) + \cos(\pi y)$, by employing our approach and the one proposed in [39, Section 2.1-2.2]. In the latter work, the projection of f_A is evaluated by computing the intersections between a tetrahedral acoustic grid and a tetrahedral fluid grid and then using a mid-point quadrature rule on the intersected elements.

We consider a domain $\Omega = \Omega_F = \Omega_A = (-4, 4) \times (-4, 4) \times (-0.05, 0.05)$, a Cartesian mesh $\mathcal{T}_F$ with 400×400 elements, and two acoustic grids with 32×32 elements, namely a non-nested Cartesian grid $\mathcal{T}_{Ac}$ and a morphed Cartesian grid $\mathcal{T}_{Am}$, see Figure 11. Next, we compute the intersections by means of Algorithm 1 and use either a mid-point quadrature rule or the quadrature-free method in Section 4.2. The obtained results are reported in Table 3. As one can see, for polynomial degree $r = 1$ both integration methods lead to the same results while for $r = 2$ the proposed approach outperforms the mid-point quadrature rule used in [39]. This is in agreement with the theoretical results in Section 4.2.

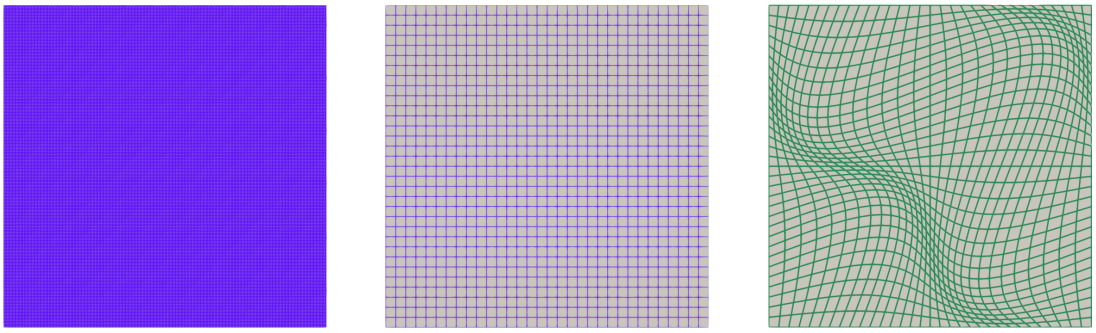

(a) Cartesian grid $\mathcal{T}_F$. (b) Cartesian grid $\mathcal{T}_{Ac}$. (c) Morphed grid $\mathcal{T}_{Am}$.

Figure 11: Employed grids for the verification test in Table 3.

	$\mathcal{T}_{Ac}$		$\mathcal{T}_{Am}$	
	$r = 1$	$r = 2$	$r = 1$	$r = 2$
Proposed L^2 projection method	1.976×10^{-2}	2.034×10^{-3}	3.047×10^{-2}	3.691×10^{-3}
Mid point [39]	1.976×10^{-2}	2.567×10^{-1}	3.068×10^{-2}	8.948×10^{-1}

Table 3: Computed $\left\| f - f_A \right\|_{L^2(\Omega)}$ error on different grid configuration.

7 Aeroacoustic Applications

In this section we apply the developed aeroacoustic hybrid strategy to relevant aeroacoustic benchmark problems. First, we test our strategy on a benchmark having an analytical solution, namely, the corotating vortex pair. This problem has been largely employed as a benchmark for aeroacoustic problems, see for instance [32], [27] or [25]. Next, we consider the noise induced by the two-dimensional laminar flow around a squared cylinder.

7.1 Corotating vortex pair

We apply our hybrid aeroacoustic computational strategy to the corotating vortex pair problem. For this test case the fluid solution can be computed analytically based on potential flow theory. Furthermore, an analytical expression for the pressure fluctuations is obtained at the far field, for a detailed derivation of the analytical solution see [33] or [32]. We assume that the flow field induced by the corotating vortex pair is inviscid and incompressible. This assumption allows us to employ a complex potential function $\Phi(z,t) : \mathbb{C} \times (0,T] \to \mathbb{C}$ to describe the flow field, namely:

$$\Phi(z,t) = \frac{\Gamma}{2\pi i} \ln(z - b(t)) + \frac{\Gamma}{2\pi i} \ln(z + b(t)), \tag{42}$$

where Γ is the circulation, i is the imaginary unit and $b = r_0 \exp(i\omega t) \in \mathbb{C}$ are the rotating centres of the vortexes, where ω is the rotational speed defined as $\omega = \Gamma/(4\pi r_0^2)$ and r_0 is the distance with respect to the origin axes, see Figure 12. We introduce the rotating Mach number $M_r = \Gamma/(4\pi r_0 c_0)$, where c_0 is the speed of the wave. The period of the rotating monopoles is $T_F = 8\pi^2 r_0^2/\Gamma$, while the emitted period of the acoustic wave is $T_A = T_F/2$. From the complex potential in (42) we compute the two-dimensional fluid flow velocity $\mathbf{u} = [u; v]$ as

$$u - iv = \frac{\partial}{\partial z} \Phi(z,t), \tag{43}$$

Γ [m s^{-2}]	M_r	T_A [s]	r_0 [m]
0.98696	0.0785397	40	1
ρ_0 [km^{-3}]	c_0 [m s^{-1}]	ω [s^{-1}]	r_c [m]
1	1	0.0785397	0.2

Table 4: Parameters employed for the rotating vortex pair test case.

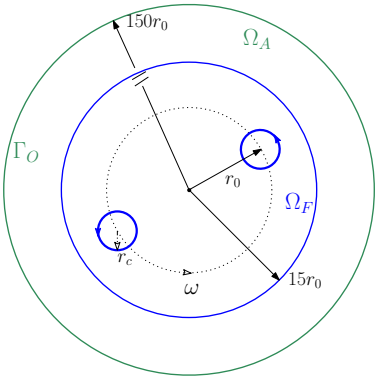

Figure 12: Sketch of the domain for the corotating vortex pair problem.

and then we compute the Lighthill's stress tensor. We report the far field solution for the pressure fluctuations $p' = p - \overline{p}$, see for instance [37]:

$$p'(z,t) = -\frac{\rho_0 c_0^2}{64\pi^3}\left(\frac{\Gamma}{r_0 c_0}\right)^4 [J_2(kr)\sin(2(\theta-\omega t) + Y_2(kr)\cos(2\theta-\omega t)], \tag{44}$$

where J_2 and Y_2 are respectively the first and second type Bessel functions, $k = 2\omega/c_0$ and $z = r\exp(i\theta)$. As already showed in [27], a desingularization model is required in order to avoid numerical issues in representing the source vortexes. Here, we employ the Scully model [41] getting

$$u_\theta(r_v) = \frac{\Gamma r_v}{2\pi(r_c^2 + r_v^2)}, \tag{45}$$

where r_c is the desingularized core radius, $u_\theta(r_v)$ is the tangential velocity and r_v is the distance with respect to the vortex core center.

Fluid Setup

We consider the corotating vortex pair problem with the parameters summarized in Table 4. The fluid domain is a circle Ω_F with radius $15r_0$. The flow solution is computed by employing the complex velocity in (43) and then the Lighthill's tensor $\nabla\cdot\mathbf{T} = \rho_0\nabla\cdot(\mathbf{u}\otimes\mathbf{u})$ as a post-process of the flow velocity, see Section 2.3. The solutions are saved at each time instant with time step $\Delta t_F = 0.02$. Since the solution is periodic, we store the solutions up to T_A.

Acoustic Setup

The acoustic domain Ω_A is a circle of radius $150r_0$. On the external boundary Γ_O absorbing conditions are imposed. We employ a polynomial degree $r = 2$ for the SE discretization. We consider a structured grid meshing strategy with a total of 57500 elements. Each vortex has around at least 15 elements. For the time discretization, an implicit Newmark method

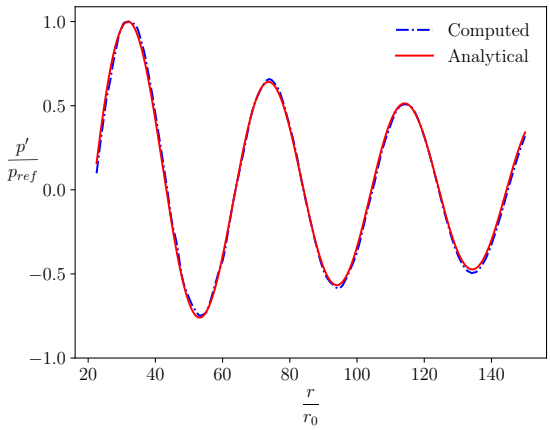

Figure 13: Comparison between the analytical far field solution and the computed numerical solution obtained with the hybrid approach and by employing the vortex core model. The results have been normalized with respect to $p_{ref} = \max(p - \overline{p})$ to take into account the energy disparity introduced by the vortex model.

is used, see for instance [24] or [4], with $\beta = 0.5, \alpha = 0.25$ and $\Delta t_A = 0.02$. In order to avoid spurious oscillation due to the non-consistent initial conditions, see [14] or [29], the following time ramp is multiplied by the source term $f(t) = \frac{1}{2}\left(1 - \cos\left(\pi \frac{t}{T_f}\right)\right)$, where $T_f = T_A$, up to T_f.

Numerical results

The acoustic field generated by a pair of corotating vortices is a rotating acoustic quadrupole as can be seen from Figure 14. The numerical solution obtained through the proposed algorithm matches the analytical solution as it is shown in Figure 13, where we sampled the pressure fluctuations p' along the line $y = 0$ with $x > 0$ at $T = 380\,\mathrm{s}$. The results obtained with the analytical solution have been normalized to a reference pressure $p_{ref} = \max(p')$ in order to take into account the desingularization effect in (45), see for instance [38].

7.2 Flow around a squared cylinder at low Reynolds number

Finally, we consider the case of a laminar flow around a square cylinder, see for instance the Direct Numerical Simulation (DNS) performed by [22] or the solution obtained with a Curle analogy in [1]. When a rigid squared cylinder is placed in a uniform flow, it exhibits strong vortex shedding, resulting in fluctuating forces due to the alternating pressure highs and drops at the wake. These forces and the turbulence in the wake generate noise. For laminar flows, the main frequency radiated from the body is associated with the Strouhal number and the intensity of the observed noise is proportional to the fluctuation of the forces. The flow solution has been computed by employing the Pressure Implicit Splitting Operator (PISO) method implemented in OpenFOAM [46].

Fluid Setup

A laminar two-dimensional incompressible simulation of a fluid flow around a square cylinder is performed. Let $D = 3.28 \times 10^{-5}$ m be the length of the square cylinder, $U = 68.7\,\mathrm{m\,s^{-1}}$ be the inlet velocity and $\nu = 1.5 \times 10^{-5}\mathrm{m^2\,s^{-1}}$ the kinematic viscosity. The Reynolds number

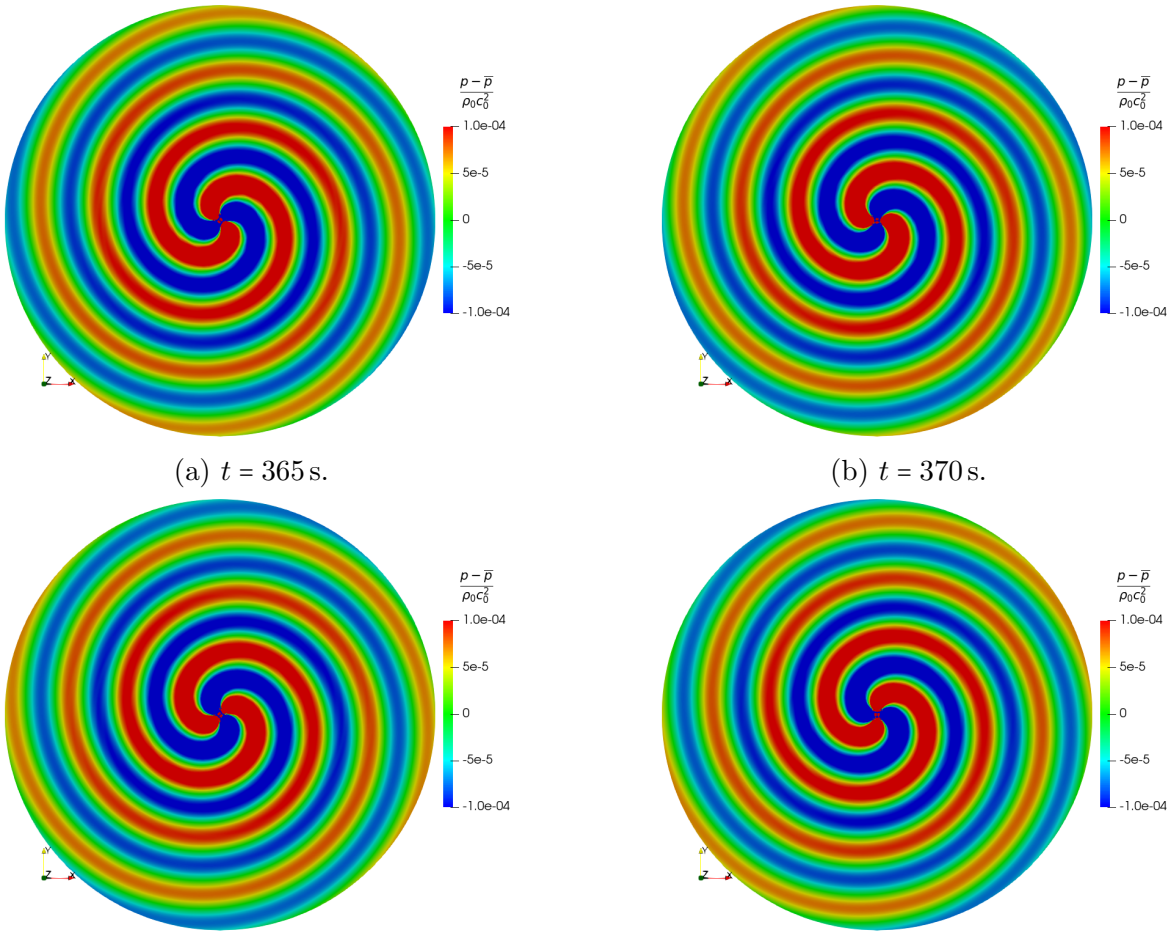

(a) $t = 365\,\mathrm{s}$. (b) $t = 370\,\mathrm{s}$.

(c) $t = 375\,\mathrm{s}$. (d) $t = 380\,\mathrm{s}$.

Figure 14: Snapshots of the computed numerical solution for the corotating vortex pair for $t = 365, 370, 375, 380$ s.

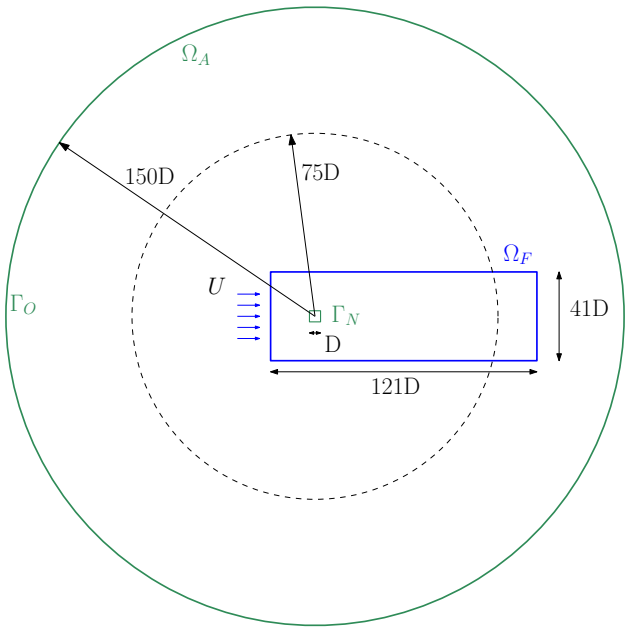

Figure 15: Computational domain of the fluid problem and the acoustic problem. The square cylinder has a diameter $D = 3.28 \times 10^{-5}$m and the fluid domain is a rectangle of size $121D \times 41D$. The acoustic domain is a circle of radius $150D$, centered at the centre of the square. The dotted line represent the sampled probes in the acoustic domain employed to compute the directivity, see Fig. 18.

is Re = 150 and the Mach number is Ma = 0.2. The fluid computational domain Ω_F is $(-20.5D, 100.5D) \times (-20.5D, 20.5D)$, see Figure 15. A fixed velocity U is prescribed at the inlet. On the upper and lower wall symmetry conditions are employed. No slip conditions are applied on the cylinder walls. Zero gradient pressure conditions are applied at the wall of the cylinder and at the inlet. On the outlet, the pressure is set to zero, while a zero gradient condition is imposed for the velocity. A block structured h-grid around the square cylinder is used, employing 970000 elements. The computational time step is $\Delta t = 10^{-9}$s.

Acoustic Setup

The acoustic domain Ω_A is a circle of radius $150D$ with an internal square hole of side D, see Figure 15. On the external boundary Γ_O, absorbing conditions are employed. On the solid wall Γ_N Neumann boundary conditions are imposed. The coupling region is given by $\Omega_A \cap \Omega_F = \Omega_F$. A smoothing function is employed in order to let the sound source term decay to avoid the well known spurious noise generation due to the abrupt domain cut on the wake, see for instance [34] or [30]. We used the following spatial smoothing function:

$$g(x) = \begin{cases} 1 & x < r_i, \\ \frac{1}{2}\left(1 + \cos(\pi \frac{x - r_i}{r_o - r_i})\right) & x \geq r_i, \end{cases}$$

where r_i is the initial filtering position, while r_o is the end of the fluid domain. In this case, it is sufficient to apply the smooth function only downstream and along the x direction, so that $r_i = 65D$ and $r_o = 105.5D$. The fluid solution is sampled every 10 fluid time steps, meaning that $\Delta t_A = 10^{-8}\text{s} = 10\Delta t_F$. The expected main frequency is the Strouhal frequency. The acoustic discretization close to the square is h-type, with $h_A = D/10$. Then the grid is

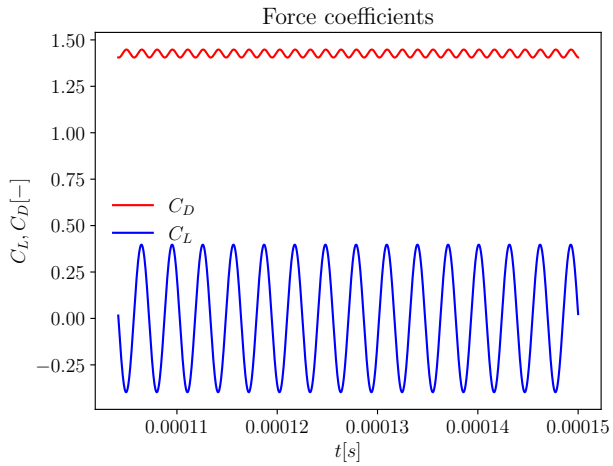

Figure 16: Computed C_L and C_D coefficients.

unstructured and a o-type grid is employed. The polynomial degree chosen is $r = 2$. The whole acoustic grid has around 420600 degrees of freedom. The main wavelength associated to the lift force is $\lambda \approx 32.5D$ and around 40 nodes per wavelength where placed in the far field. The acoustic simulation was run for 0.00005s, starting from a fluid time of $t_F = 0.0001\,\mathrm{s}$, hence with a fully developed flow field.

Numerical results

$C_D = \dfrac{F_D}{\frac{1}{2}\rho_0 U^2 A}$ and $C_L = \dfrac{F_L}{\frac{1}{2}\rho_0 U^2 A}$, where F_D and F_L are the drag and lift forces respectively, with $A = D \times H$, being H the width of the domain and having chosen $H = D$, we plot C_L and C_D in Figure 16. We introduce the Strouhal number $St = f\dfrac{D}{U}$, with f being the frequency of the C_L. In Table 5 we compare our results with those available in the literature. The obtained Strouhal number matches the results obtained by [11] and they are aligned with the experiments [35, 42] and the compressible DNS performed by [22]. The intensity of the noise emitted by the square cylinder depends mainly on the fluctuations of the forces. Hence, during the flow computation it is critical to match the root means squared (rms) values. By defining $\overline{C}_D$ as the average of C_D, respectively C_L, we compute the rms values as $C_{L,rms} = \sqrt{\overline{(C_L - \overline{C}_L)^2}}$ and we also identify $C_{L,peak} = \max(|C_L|)$. Again, from Table 5 we see that out results are in agreement with the ones available in literature. Finally, we compute the acoustic field, namely the noise induced by the flow around the square cylinder. From Figure 17, we see the characteristic dipole pattern, that is mainly due to the lift force acting on the cylinder. The obtained results are comparable with the compressible simulations, see for instance [10] and [22]. To further validate the obtained acoustic results, we computed the directivity from $p'_{rms} = \sqrt{\overline{(p - \overline{p})^2}}$. The obtained directivity pattern is in good agreement with the references, see [22] and [1].

8 Conclusion

We proposed a hybrid computational strategy that couples a finite volume flow solver with a high order acoustic solver for aeroacoustic simulations. First, the fluid flow solution is computed employing the open-source finite volume library OpenFOAM. Then, a post-

	St	$\overline{C}_D$	$C_{L,rms}$	$C_{L,peak}$
Experiments [35, 42]	0.148-0.155	1.4	-	-
Doolan [11]	0.156	1.44	0.296	-
Ali [1]	0.16	1.47	0.285	-
Inoue [22]	0.151	1.4	-	0.4
Current study	0.156	1.43	0.281	0.3976

Table 5: Comparison of the flow results with analogous results available in literature.

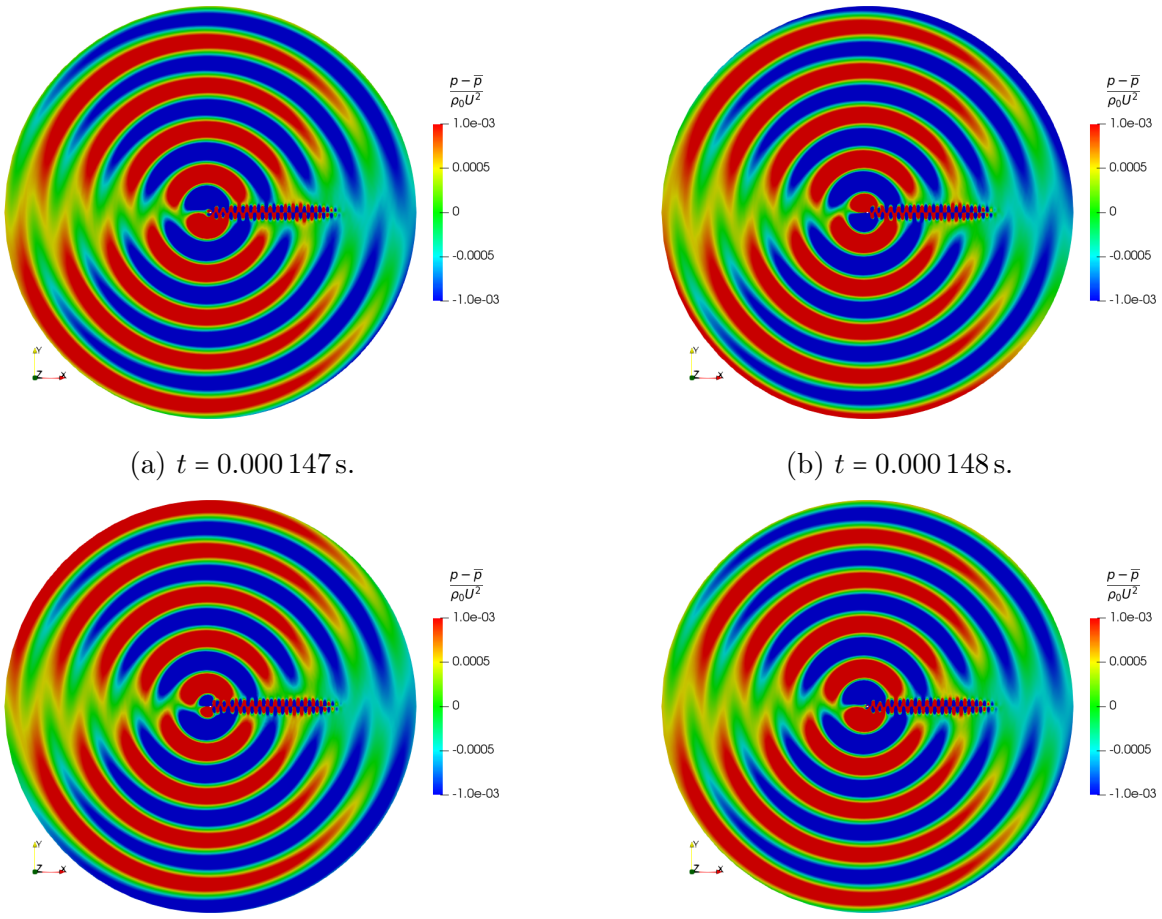

(a) $t = 0.000\,147$ s.

(b) $t = 0.000\,148$ s.

(c) $t = 0.000\,149$ s.

(d) $t = 0.000\,15$ s.

Figure 17: Snapshot of the computed acoustic pressure field at t = 0.000147, 0.000148, 0.000149, 0.00015 s.

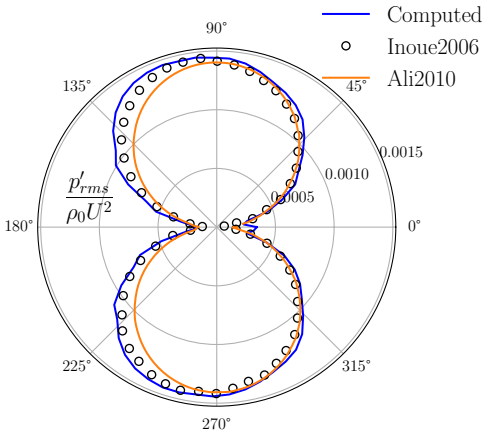

Figure 18: Directivity pattern. The adimensionalized p'_{rms} has been sampled on a circumference of radius 75D, see Fig. 1. Comparison with the DNS in [22] and the Curle computations of [1].

processing of the flow solution computes the sound source term on the fluid grid, by means of the Lighthill's acoustic analogy. Next, a projection method is used to map the flow source term from the fluid to the acoustic grid. Finally, an inhomogeneous wave equation is solved by employing a high-order spectral element method. The employed projection method exploited a robust intersection algorithm that is able to perform the intersection between the two computational grids. Furthermore, we employed a quadrature free method to integrate polynomial functions over the generic polyhedral elements stemming after the intersections computation. We explored the computational aspects of the proposed intersection algorithm both from a theoretical and numerical point of view. Finally, we applied the developed computational strategy to different aeroacoustic problems, showing the effectiveness of the proposed method.

9 Acknowledgements

The authors thank prof. M. Verani, prof. Corradi and Dr. Schito for the insightful discussions on the topic. The simulations have been partly run at Cineca thanks to the computational resources made available through the HO-AERO HP10C9XBN9 ISCRA-C project. The authors are members of the INdAM Research Group GNCS. P.F.A. has been partially funded by the research projects PRIN n. 201744KLJL, funded by MIUR, and P.F.A. and N.P. have been partially supported by PRIN n. 20204LN5N5 research grant funded by MIUR. P.F.A., I.M. and N.P. have been partially funded by European Union - Next Generation EU.

References

[1] M. Ali, M. Sukri, C. Doolan, and V. Wheatley. "Aeolian tones generated by a square cylinder with a splitter plate". In: *Journal of Sound and Vibration* (Jan. 2010).

[2] F. Alipour, C. Brücker, D. D. Cook, A. Gommel, M. Kaltenbacher, W. Mattheus, L. G. Mongeau, Eric A. Nauman, Rüdiger Schwarze, I. T. Tokuda, and S. Zörner. "Mathematical Models and Numerical Schemes for the Simulation of Human Phonation". In: *Current Bioinformatics* 6 (2011), pp. 323–343.

[3] P. Antonietti, P. Houston, G. Pennesi, and E. Süli. "An agglomeration-based massively parallel non-overlapping additive Schwarz precondition er for high-order discontinuous Galerkin methods on polytopic grids". In: *Mathematics of Computation* 89 (Nov. 2019), p. 1.

[4] P. Antonietti, I. Mazzieri, M. Muhr, V. Nikolić, and B. Wohlmuth. "A high-order discontinuous Galerkin method for nonlinear sound waves". In: *Journal of Computational Physics* 415 (2020), p. 109484.

[5] P. F. Antonietti, P. Houston, and G. Pennesi. "Fast Numerical Integration on Polytopic Meshes with Applications to Discontinuous Galerkin Finite Element Methods". In: *Journal of Scientific Computing* 77.3 (Dec. 2018), pp. 1339–1370.

[6] C.G. Canuto, Mohammed Hussaini, A. Quarteroni, and T. Zang. *Spectral Methods: Evolution to Complex Geometries and Applications to Fluid Dynamics*. Ed. by Springer. 2007.

[7] S. Caro, Y. Detandt, J. Manera, F. Mendonça, and R. Toppinga. "Validation of a New Hybrid CAA Strategy and Application to the Noise Generated by a Flap in a Simplified HVAC Duct". In: *15th AIAA/CEAS Aeroacoustics Conference (30th AIAA Aeroacoustics Conference)* (May 2009).

[8] E. B. Chin, J. B. Lasserre, and N. Sukumar. "Numerical integration of homogeneous functions on convex and nonconvex polygons and polyhedra". In: *Computational Mechanics* 56.6 (Dec. 2015), pp. 967–981.

[9] N. Curle and M. J. Lighthill. "The influence of solid boundaries upon aerodynamic sound". In: *Proceedings of the Royal Society of London. Series A. Mathematical and Physical Sciences* 231.1187 (1955), pp. 505–514.

[10] V. D'Alessandro, M. Falone, L. Giammichele, and S. Montelpare. "A low—storage Runge—Kutta OpenFOAM solver for compressible low—Mach number flows: aeroacoustic and thermo—fluid dynamic applications". In: *E3S Web of Conferences* 128 (Jan. 2019), p. 10001.

[11] C. J. Doolan. "Flat-Plate Interaction with the Near Wake of a Square Cylinder". In: *AIAA Journal* 47.2 (2009), pp. 475–479.

[12] D. Eberly. *Robust and Error-Free Geometric Computing*. London: CRC Press, 2020.

[13] B. Engquist and A. Majda. "Absorbing boundary conditions for the numerical simulation of waves". English (US). In: *Mathematics of Computation* 31.139 (July 1977), pp. 629–651.

[14] M. Escobar. "Finite Element Simulation of Flow-Induced Noise using Lighthill's Acoustic Analogy". In: *Ph.D. Thesis* (2007).

[15] R. Ewert and W. Schröder. "Acoustic perturbation equation based on flow decomposition via source filtering". In: *Journal of Computational Physics* 188 (July 2003), pp. 365–398.

[16] S. Falk, S. Kniesburges, S. Schoder, B. Jakubaß, P. Maurerlehner, M. Echternach, M. Kaltenbacher, and M. Döllinger. "3D-FV-FE Aeroacoustic Larynx Model for Investigation of Functional Based Voice Disorders". In: *Frontiers in Physiology* 12 (Mar. 2021).

[17] Joel H. Ferziger and Milovan Perić. *Computational Methods for Fluid Dynamics*. 2nd. Berlin: Springer, 1999.

[18] J. E. Ffowcs Williams, D. L. Hawkings, and M. J. Lighthill. "Sound generation by turbulence and surfaces in arbitrary motion". In: *Philosophical Transactions of the Royal Society of London. Series A, Mathematical and Physical Sciences* 264.1151 (1969), pp. 321–342.

[19] H. M. Frank and C.D. Munz. "Direct aeroacoustic simulation of acoustic feedback phenomena on a side-view mirror". In: *Journal of Sound and Vibration* 371 (2016), pp. 132–149.

[20] P. Hachenberger and L. Kettner. "3D Boolean Operations on Nef Polyhedra". In: *CGAL User and Reference Manual*. 5.4. CGAL Editorial Board, 2022.

[21] A. Huppe. “Spectral Finite Elements for Acoustic Field Computation”. In: *Ph.D. Thesis* (Dec. 2012).

[22] O. Inoue, M. Mori, and N. Hatakeyama. “Aeolian tones radiated from flow past two square cylinders in tandem”. In: *Physics of Fluids* 18.4 (2006).

[23] B. Kaltenbacher, M. Kaltenbacher, and I. Sim. “A modified and stable version of a perfectly matched layer technique for the 3-d second order wave equation in time domain with an application to aeroacoustics”. In: *Journal of computational physics* 235 (Feb. 2013), pp. 407–422.

[24] M. Kaltenbacher. *Numerical simulation of mechatronic sensors and actuators*. Vol. 2. Springer, 2007.

[25] M. Kaltenbacher, M. Escobar, S. Becker, and I. Ali. “Computational Aeroacoustics based on Lighthill’s Acoustic Analogy”. In: *Computational Acoustics of Noise Propagation in Fluids - Finite and Boundary Element Methods*. Berlin, Heidelberg: Springer Berlin Heidelberg, 2008, pp. 115–142.

[26] M. Kaltenbacher, M. Escobar, S. Becker, and I. Ali. “Numerical simulation of flow-induced noise using LES/SAS and Lighthill’s acoustic analogy”. In: *International Journal for Numerical Methods in Fluids* 63.9 (2010), pp. 1103–1122.

[27] D. J. Lee and S. O. Koo. “Numerical study of sound generation due to a spinning vortex pair”. In: *AIAA Journal* 33.1 (1995), pp. 20–26.

[28] M. J. Lighthill and M. H. A. Newman. “On sound generated aerodynamically I. General theory”. In: *Proceedings of the Royal Society of London. Series A. Mathematical and Physical Sciences* 211.1107 (1952), pp. 564–587.

[29] Y.S.K. Liow, B.T. Tan, M.C. Thompson, and K. Hourigan. “Sound generated in laminar flow past a two-dimensional rectangular cylinder”. In: *Journal of Sound and Vibration* 295.1 (2006), pp. 407–427.

[30] P. Martínez-Lera and C. Schram. “Correction techniques for the truncation of the source field in acoustic analogies”. In: *The Journal of the Acoustical Society of America* 124 (6 Dec. 2008).

[31] I. Mazzieri, M. Stupazzini, R. Guidotti, and C. Smerzini. “SPEED: SPectral Elements in Elastodynamics with Discontinuous Galerkin: a non-conforming approach for 3D multi-scale problems”. In: *International Journal for Numerical Methods in Engineering* 95.12 (2013), pp. 991–1010.

[32] B. E. Mitchell, S. K. Lele, and P. Moin. “Direct computation of the sound from a compressible co-rotating vortex pair”. In: *Journal of Fluid Mechanics* 285 (1995), 181–202.

[33] E. A. Muller and F. Obermeier. “The spinning vortices as a source of sound”. In: *AGARD CP-22* 22 (1967).

[34] A. A. Oberai, F. Roknaldin, and T. J.R. Hughes. “Computational procedures for determining structural-acoustic response due to hydrodynamic sources”. In: *Computer Methods in Applied Mechanics and Engineering* 190.3 (2000), pp. 345–361.

[35] A. Okajima. “Strouhal numbers of rectangular cylinders”. In: *Journal of Fluid Mechanics* 123 (Oct. 1982), pp. 379–398.

[36] A. Quarteroni. *Numerical models for differential problems; 1st ed.* Milano: Springer, 2009.

[37] M. Schlottke-Lakemper. “A direct-hybrid method for aeroacoustic analysis”. In: *Ph.D. Thesis* (2017).

[38] M. Schlottke-Lakemper, M. Meinke, and W. Schröder. “A Hybrid Discontinuous Galerkin-Finite Volume Method for Computational Aeroacoustics”. In: *New Results in Numerical and Experimental Fluid Mechanics X*. Cham: Springer International Publishing, 2016, pp. 743–753.

[39] S. Schoder, A. Wurzinger, C. Junger, M. Weitz, C. Freidhager, K. Roppert, and M. Kaltenbacher. “Application Limits of Conservative Source Interpolation Methods Using a Low Mach Number Hybrid Aeroacoustic Workflow”. In: *Journal of Theoretical and Computational Acoustics* 29.01 (2021), p. 2050032.

[40] Christoph Schwab. *P- and hp- finite element methods : theory and applications in solid and fluid mechanics*. 1998.

[41] Michael Scully. “Computation of helicopter rotor wake geometry and its influence on rotor harmonic airloads”. In: (1975).

[42] A. Sohankar, C. Norberg, and L. Davidson. “Simulation of three-dimensional flow around a square cylinder at moderate Reynolds numbers”. In: *Physics of Fluids* 11.2 (1999), pp. 288–306.

[43] Michael E. Taylor. *Partial Differential Equations I, Basic Theory*. New York: Springer, 1996.

[44] The CGAL Project. *CGAL User and Reference Manual*. 5.5.1. CGAL Editorial Board, 2022. URL: `https://doc.cgal.org/5.5.1/Manual/packages.html`.

[45] Y.S. Wang, L.N. Sui, Z.Y. Yin, X.L. Wang, N.N. Liu, and H. Guo. "A hybrid prediction for wind buffeting noises of vehicle rear window based on LES-LAA method". In: *Applied Mathematical Modelling* 47 (2017), pp. 160–173.

[46] H. G. Weller, G. Tabor, H. Jasak, and C. Fureby. "A tensorial approach to computational continuum mechanics using object-oriented techniques". In: *Computers in Physics* 12.6 (1998), pp. 620–631.

[47] W. Zheng and H. Qi. "On Friedrichs–Poincaré-type inequalities". In: *Journal of Mathematical Analysis and Applications* 304 (Apr. 2005), pp. 542–551.

[48] P. Šidlof, S. Zörner, and A. Hüppe. "A hybrid approach to the computational aeroacoustics of human voice production". In: *Biomechanics and modeling in mechanobiology* 14 (Oct. 2014).

MOX Technical Reports, last issues

Dipartimento di Matematica
Politecnico di Milano, Via Bonardi 9 - 20133 Milano (Italy)

05/2023 Fumagalli, I.; Vergara, C.
Novel approaches for the numerical solution of fluid-structure interaction in the aorta

04/2023 Quarteroni, A.; Dede’, L.; Regazzoni, F.; Vergara, C.
A mathematical model of the human heart suitable to address clinical problems

01/2023 Zingaro, A.; Bucelli, M.; Piersanti, R.; Regazzoni, F.; Dede', L.; Quarteroni, A.
An electromechanics-driven fluid dynamics model for the simulation of the whole human heart

03/2023 Africa, P.C.; Perotto, S.; de Falco, C.
Scalable Recovery-based Adaptation on Quadtree Meshes for Advection-Diffusion-Reaction Problems

02/2023 Boon, W. M.; Fumagalli, A.; Scotti, A.
Mixed and multipoint finite element methods for rotation-based poroelasticity

85/2022 Lurani Cernuschi , A.; Masci, C.; Corso, F.; Muccini, C.; Ceccarelli, D.; San Raffaele Hospital Galli, L.; Ieva, F.; Paganoni, A.M.; Castagna, A.
A neural network approach to survival analysis for modelling time to cardiovascular diseases in HIV patients with longitudinal observations

83/2022 Ciaramella, G.; Gander, M.; Mazzieri, I.
Unmapped tent pitching schemes by waveform relaxation

81/2022 Bonizzoni, F.; Hauck, M.; Peterseim, D.
A reduced basis super-localized orthogonal decomposition for reaction-convection-diffusion problems

82/2022 Ciaramella, G.; Gander, M.; Van Criekingen, S.; Vanzan, T.
A PETSc Parallel Implementation of Substructured One- and Two-level Schwarz Methods

84/2022 Ciaramella, G.; Gambarini, M.; Miglio, E.
A preconditioner for free-surface hydrodynamics BEM